Apoptosis (2025) 30:1589–1613
https://doi.org/10.1007/s10495-025-02119-8

GJB2 as a novel prognostic biomarker associated with immune infiltration and cuproptosis in ovarian cancer

Han Lei[1] · Ke Guo[3] · Guang Shu[1] · Maonan Wang[1] · Yu Li[4] · Zhihui Tan[5] · Qiong Pan[2] · Gang Yin[1,6,7]

Accepted: 17 April 2025 / Published online: 15 May 2025

Abstract

Cuproptosis, a recently identified copper-dependent cell death mechanism, remains poorly unexplored in ovarian cancer (OC). This study systematically evaluates clinically significant cuproptosis-related genes (CRGs) as potential prognostic biomarkers in OC. Cox regression analysis and LASSO algorithms were used to develop a prognostic risk model incorporating 5 CRGs (*CD8B2*, *GJB2*, *GRIP2*, *MELK*, and *PLA2G2D*) within the TCGA cohort. This model stratified OC patients into high-risk and low-risk groups, with the high-risk group exhibiting significantly shorter overall survival compared to the low-risk group. The model's predictive accuracy for prognosis in OC patients was validated in the TCGA training cohort, TCGA testing cohort, and ICGC external validation cohorts. Among these 5 signature genes, the number of cuproptosis genes associated with *GJB2* is the largest, so we selected *GJB2* for further validation. qPCR revealed that *GJB2* was highly expressed in OC cells and tumor tissues. The high expression of *GJB2* was closely associated with poor prognosis in OC patients. Functionally, *GJB2* silencing suppressed OC cell proliferation and migration while its overexpression promoted malignant progression and EMT. Furthermore, *GJB2* regulated copper homeostasis and reduced cuproptosis sensitivity, while also facilitating immune escape by inhibiting $CD8^+$ T cell infiltration and cytokine secretion, revealing its multiple roles in OC progression. In conclusion, we established a novel prognostic model incorporating 5 CRGs that effectively predicts clinical outcomes and characterizes the immune microenvironment in OC. Our findings particularly highlight *GJB2* as a key regulator of cuproptosis with significant potential as both a prognostic biomarker and therapeutic target for OC management.

Keywords Ovarian cancer · Prognostic signature · *GJB2* · Proliferation and migration · Cuproptosis · Immune infiltration

✉ Zhihui Tan
tanzhihui@csu.edu.cn

✉ Qiong Pan
1517682924@qq.com

✉ Gang Yin
gangyin@csu.edu.cn

[1] Department of Pathology, Xiangya Hospital, School of Basic Medical Sciences, Central South University, Changsha, China

[2] Department of Obstetrics and Gynecology, The Third Xiangya Hospital of Central South University, Changsha, China

[3] Department of Neurology, The Third Xiangya Hospital of Central South University, Changsha, China

[4] Intensive Care Unit for Children, Xiangtan Central Hospital, Xiangtan, China

[5] Department of Gynecology, Xiangya Hospital, Central South University, Changsha, China

[6] China-Africa Research Center of Infectious Diseases, School of Basic Medical Sciences, Central South University, Changsha, China

[7] National Clinical Research Center for Geriatric Disorders, Xiangya Hospital, Central South University, Changsha, China

Abbreviations

OC	Ovarian cancer
TCGA	The cancer genome atlas
GTEx	Genotype tissue expression
ICGC	International cancer genome consortium
CGs	Cuproptosis genes
DEGs	Differentially expressed genes
DECGs	Differentially expressed cuproptosis genes
CRGs	Cuproptosis-related genes
CNVs	Copy number variations
LASSO	Least absolute shrinkage and selection operator
OS	Overall survival
KM	Kaplan–Meier
ROC	Receiver operating characteristic
AUC	Areas under the curve
PCA	Principal component analysis
t-SNE	T-distributed Stochastic Neighbor Embedding
C-index	Concordance index
IC50	Half-maximal inhibitory concentration
TIDE	Tumor immune dysfunction and exclusion
ICI	Immune checkpoint inhibitor
TIS	Tumor inflammation signature
CSCs	Cancer stem cells
GO	Gene ontology
GSVA	Gene set variation analysis
GDSC	Genomics of drug sensitivity in cancer
GSCA	Gene set cancer analysis
TCIA	The cancer immunome atlas
IOSE	Immortalized ovarian surface epithelial
OE	Overexpression
NC	Negative control
GJB2	Gap junction protein beta-2
Cx26	Connexin 26
TMB	Tumor mutation burden
TME	Tumor microenvironment
TIME	Tumor immune microenvironment
EMT	Epithelial-mesenchymal transition

Introduction

Ovarian cancer (OC) is the second highest cause of mortality in gynecological malignancies worldwide, and its high mortality is mainly related to the difficulty of early diagnosis, high aggressiveness, and the development of chemotherapy resistance [1]. Due to the absence of distinctive symptoms and reliable biomarkers, most patients are diagnosed at advanced stages [2]. Despite advances in treatments such as targeted therapy and immunotherapy, the 5-year overall survival rate remains low, largely due to recurrence, drug resistance, and therapeutic uncertainty [3–5]. In clinical applications, the accurate assessment of prognosis in cancer patients relies on molecular biomarkers, which can help identify clinical risk groups and guide treatment decisions, making them a crucial component of personalized therapy [6].

Emerging evidence demonstrates that dysregulated copper homeostasis plays a pivotal role in cancer pathogenesis across multiple malignancies [7, 8]. Some studies have shown that decreased serum copper concentrations are linked to the development of endometrial cancer [9], and an imbalance in copper homeostasis has also been observed in the progression of head and neck cancers [10]. Recently, a groundbreaking study by Tsvetkov et al. identified a novel form of copper-dependent cell death, termed cuproptosis [11]. This mechanism, previously unidentified, has significant implications for understanding new regulatory pathways in cancer. While this breakthrough has opened new avenues for exploring copper-mediated regulatory networks in cancer biology, the potential connection between cuproptosis and OC pathogenesis remains largely speculative, with no definitive mechanistic evidence currently available to substantiate this relationship in OC models or clinical samples.

Gap Junction Protein Beta 2 (*GJB2*), also known as connexin 26 (*Cx26*), is a member of the connexin family and plays a key role in the formation of hemichannels and gap junctions. The opening of hemichannels facilitates the release of signaling molecules, such as ATP and glutamate, into the extracellular space [12]. Emerging evidence demonstrates that aberrant *GJB2* expression disrupts gap junction intercellular communication (GJIC) across multiple malignancies, including breast, colorectal, and non-small cell lung cancers [13–15]. Beyond its canonical role in GJIC, connexins have been shown to orchestrate cancer progression through hemichannel-mediated modulation of autocrine/paracrine signaling networks [16]. Previous studies have shown that GJIC mediated by *Cx26* promotes tumorigenesis by regulating cell proliferation and differentiation, while also enhancing cancer cell migration by reducing tumor cell adhesion [17, 18]. Teleki et al. [19] reported that *GJB2* expression was downregulated after chemotherapy in breast cancer patients, suggesting an association between *GJB2* expression and chemotherapy response, and highlighting its potential as an anti-cancer drug target. Although significant progress has been made in understanding *GJB2* functions in other cancer types, its pathophysiological roles in OC, particularly the specific mechanisms underlying therapy resistance, metastasis, and tumor microenvironment modulation, remain completely uncharted territory.

This study aimed to identify predictive cuproptosis-related genes (CRGs) in OC that can not only provide valuable insight into the molecular networks, the signaling pathway, and the tumor immune infiltration that is related

to cuproptosis in OC but can also be used to identify OC patients at high risk of poor survival. In our research, we identified 5 CRGs (*CD8B2*, *GJB2*, *GRIP2*, *MELK*, and *PLA2G2D*) and developed a prognostic model. Based on the CRG risk score, we classified the TCGA-OC patients into a high-risk group and a low-risk group. The functional role of CRGs in OC was further explored through gene set enrichment analysis (GSEA), assessing their potential for predicting prognosis, diagnosis, tumor immune infiltration, chemotherapeutic drug sensitivity, and immunotherapy efficacy, with both internal and external validations. Among these 5 signature genes, *GJB2* was associated with the largest number of cuproptosis genes, so we selected the key gene *GJB2* for further validation. To elucidate the oncogenic properties of *GJB2*, OC cells were transfected with *GJB2*-related plasmid, then performed CCK-8, colony formation assay, wound healing assay, and Transwell migration assay to evaluate the impact of *CJB2* on the proliferation and migration of cells. To further characterize the molecular mechanisms underlying *GJB2*'s oncogenic effects, we employed qPCR and Western blotting analyses to systematically evaluate its impact on the Epithelial-Mesenchymal Transition (EMT) signaling pathway activation. Simultaneously, through GO enrichment analysis of *GJB2*-correlated genes, we identified significant involvement in copper ion binding pathways, which was subsequently validated by qPCR showing marked alterations in key cuproptosis regulators following *GJB2* overexpression. Later, cell viability assays also confirmed *GJB2*'s regulatory impact on cuproptosis sensitivity. Finally, Transwell migration and flow cytometric analyses revealed that *GJB2* inhibits $CD8^+$ T cell infiltration and suppresses cytokine secretion, indicative of its role in immune evasion. Collectively, these findings establish *GJB2* as a multifaceted oncogene in OC pathogenesis, driving tumor progression through proliferative, migratory, EMT-promoting, cuproptosis-modulating, and immunoevasive mechanisms, while highlighting its potential as a prognostic biomarker and therapeutic target.

Materials and methods

Data collection

The flowchart of the study design is illustrated in Fig. 1. A total of 379 OC patients and 88 normal ovarian samples were involved in the present study. The transcriptome data of TCGA-OC was downloaded from the UCSC Xena server (https://xenabrowser.net/) [20]. A total of 88 normal ovarian tissue mRNA expression samples were downloaded from the Genotype-Tissue Expression (GTEx) database. Then converted and normalized the FPKM values of TCGA-OC (379 OC patients) and GTEx-ovary (88 normal samples) to TPM values, and finally obtained an integrated expression matrix. The "NormalizeBetweenArrays" instruction of R package "limma" was used to remove batch-specific effects in the process. The clinical information of OC cases was obtained from The Cancer Genome Atlas (TCGA) database (https://portal.gdc.cancer.gov/) [21, 22], including OS, survival status, age, grade, and stage. The summarized clinical data of the OC patients are shown in Table S1. The concrete clinical information for TCGA whole dataset OC patients is in Table S2. Study participants with incomplete clinical information were excluded. OC data for Ovarian cancer-Australia OV-AU items were collected from the International Cancer Genome Consortium (ICGC, https://icgc.org) database. A total of 85 samples were included in the column as an independent verification cohort for analysis. GSE38666, GSE105437, and GSE63885 were derived from the Gene Expression Omnibus (GEO) database (https://www.ncbi.nlm.nih.gov/geo/). These datasets were achieved from common databases, and strict guidelines were obeyed according to these databases. The 97 cuproptosis genes (CGs) were extracted from a previous study for subsequent bioinformatics analysis [11, 23–25], listed in Table S3.

Mutation, correlation analysis, and differential analysis of DECGs

Differential expression genes (DEGs) in the TCGA-OC samples and normal ovarian samples were analyzed by the "limma" package in RStudio ($|\log_2 FC|>1$, $p<0.05$). Venn diagrams were used to identify TCGA-DEGs that intersected with CGs, and the overlapping genes were defined as differentially expressed cuproptosis genes (DECGs). To identify the expression differences of DECGs between the normal and tumor samples, the R "limma" and "ggpubr" packages were used to generate the boxplots for comparison. We then utilized the "maftools" [26] R package to generate a waterfall plot that allowed us to examine the mutation frequency and mutation type of DECGs in each sample. Finally, the correlation analysis of 18 DECRs was drawn with the "corrplot" R package.

Construction and validation of cuproptosis-related prognosis model

To identify cuproptosis-related genes (CRGs), we used the "limma" package to calculate the correlation between DECGs and CRGs [27]. Using the correlation coefficient $|R|>0.4$ and $p<0.001$ as the screening criteria, a total of 1435 CRGs with expression values were obtained. We further screened the differentially expressed CRGs ($|\log_2 FC|>3$, $p<0.05$) and finally obtained 71 differentially expressed CRGs. Then

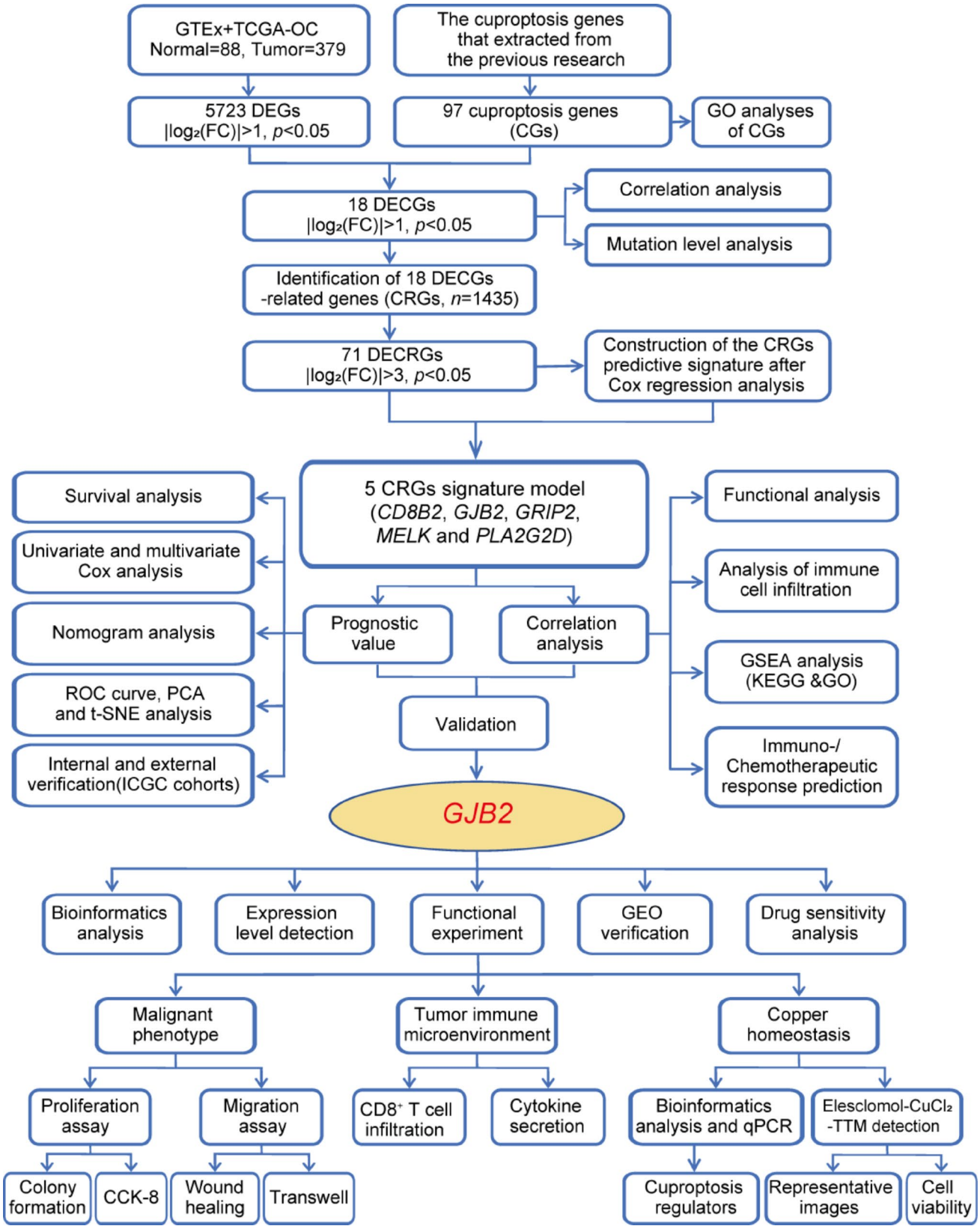

Fig. 1 Flowchart of the Study

used univariate Cox regression analysis to obtain CRGs related to the prognosis of OC patients, and we carried out multivariate Cox regression analysis and least absolute shrinkage and selection operator (LASSO) Cox regression to construct the CRGs predictive signature for OC patients. Finally, the prognostic risk model was constructed by 5 CRGs (*CD8B2*, *GJB2*, *GRIP2*, *MELK*, and *PLA2G2D*). For each patient, the risk score was calculated based on the following formula: Cuproptosis risk score = ∑(Expi × Coefi). (Expi denotes each signature gene's expression level, and Coefi denotes the corresponding coefficient).

The reliability of the prognostic signature was validated using internal validation (TCGA-OC) and external validation groups (ICGC-OC). We randomly divided all patients from the TCGA-OC database into the training and testing groups. Based on the median value of the risk score, the training group, the testing group, and all patients were classified into high-risk and low-risk groups, respectively. In both training and validation groups, the signature's predictive capability was assessed by Kaplan–Meier (KM) survival analysis and ROC curves using the "timeROC", "survival", and "survminer" R packages. Additionally, we also created a nomogram using the "survival", "rms", and "regplot" R packages to predict the 1-, 3-, and 5-year survival rates and calibrated the signature to evaluate its consistency with practice. To measure the nomogram's capacity to differentiate and predict, the concordance index (C-index) was also determined. The C-index ranged from 0.5 to 1.0, with a higher C-index indicating stronger differentiating ability of the predictive model. Additionally, we utilized the "ggplot2" R package to perform PCA analysis, which allowed us to observe the distribution of samples in the high-risk and low-risk groups.

Functional enrichment analysis and immune cell infiltration analysis

The biological processes (BP), molecular functions (MF), and cellular components (CC) of cuproptosis-related genes and *GJB2*-correlated genes were determined using Gene Ontology (GO) analysis [28] by using the clusterProfiler package [29] and org.Hs.eg.db package. Additionally, the Kyoto Encyclopedia of Genes and Genomes (KEGG) pathway analysis [30] and Gene set variation analysis (GSVA) [31] were used to investigate the pathways involved in differentially expressed genes in various risk groups. The gene sets of hallmarkers were obtained from the Molecular Signatures Database (MSigDB, http://software.broadinstitute.org/gsea/msigdb/index.jsp) for GSVA analysis.

Correlation of the prognostic signature with TME and immune checkpoints

"Reshape2", "tidyverse", "ggplot2", "ggpubr" and "ggExtra" R packages were used to analyze the correlation of risk score with immune cells and plot a heatmap depicting the relationship of signature genes with immune cells. Additionally, we compared the Tumor Microenvironment (TME) scores between high-risk and low-risk groups using the "reshape2" and "ggpubr" R packages. To further investigate the signature's predictive capability in immunotherapy response, we analyzed the expression of immune checkpoints between high-risk and low-risk groups using "limma", "ggplot2", "ggpubr" and "ggExtra" R packages [32].

Drug sensitivity analyses

Half-maximal inhibitory concentration (IC50) data for anticancer drugs were obtained from the Genomics of Drug Sensitivity in Cancer (GDSC) database (https://www.cancerrxgene.org/) [33, 34]. The drug distribution in the high-risk and low-risk score groups was analyzed and visualized using the "pRRophetic" [35] R package. The Wilcoxon sign rank test was used to compare IC50 differences between common anti-tumor drugs in the high-risk and low-risk groups. Differences in common anti-tumor drugs between high-expression and low-expression groups of *GJB2* are also analyzed using the same methods.

Protein expression in the HPA database

The Human Protein Atlas (HPA) database (https://www.proteinatlas.org/) was used for the comparison of protein expression of GJB2 between normal ovarian tissue and OC tissue samples by immunohistochemistry (IHC) [36].

Cell culture and transfection

All cell lines used in this study included human normal ovarian surface epithelial cells (Immortalized Ovarian Surface Epithelial, IOSE) and OC cell lines, HO 8910, A2780, OC314, and SKOV3 (STR identification), were cultured in RPMI-1640 (BI) replenished with 10% fetal bovine serum (FBS) (BI), 100 µg/ml penicillin (Sigma) and 100 µg/ml streptomycin (Sigma). All cells were cultured at 37 °C in a humidified 5% CO_2 incubator. Cells were collected for the experiment at the indicated time. 5×10^5 °C cells were seeded in a six-well plate and then reached 60–70% fusion degree per well, jetPRIME was applied for transient transfection plasmid and/or siRNA in vitro according to manufacturer's instructions. These cells were digested and collected after

48 h of transfection for the subsequent assays. All of the sequences of primers are listed in Table S4.

RNA isolation and qPCR

To detect the gene expression of *GJB2* and the changes resulting from *GJB2* si/OE transfection, we performed qRT-PCR analysis. Total RNA was isolated using Trizol reagent (Vazyme, Nanjing, China). Complementary DNA (cDNA) was synthesized using the TransScript Uni All-in-One First-Strand cDNA Synthesis SuperMix for qPCR (One-Step gDNA Removal) (TransGen Biotech, AU341-02-V2). qPCR was performed by the Applied Biosystems 7500 Real-Time PCR System and the ChamQ Universal SYBR qPCR Master Mix (Vazyme, Q711-02). We chose glyceraldehyde-3-phosphate dehydrogenase (*GAPDH*) to normalize *GJB2*, *CDH1*, *CDH2*, *VIM*, *FDX1*, *LIAS*, *DLAT*, and *PDHB* expression levels. Relative RNA abundances were calculated by the standard $2^{-\Delta\Delta Ct}$ method. The sequences of all qPCR primers are listed in Table S4.

Cytokine secretion assay

OC cells were seeded at a density of 1×10^5 cells per well in 12-well plates and allowed to adhere overnight. Following adhesion, cells were transfected with either *GJB2*-overexpression plasmid (*GJB2*-Flag) or empty vector control (Flag). 24 h post-transfection, OTK3-activated T cells were added to the transfected tumor cells at a 5:1 effector-to-target ratio (T cells: tumor cells). The co-culture system was maintained for 12 h, after which 500 µl of BFA/monensin solution (1 × working concentration) was added to block cytokine secretion. Following 6 h of incubation, all T cells were harvested for subsequent intracellular cytokine analysis. For cell surface and intracellular staining, cells were first incubated with APC-anti human CD8 antibody at 4 °C for 30 min in the dark for extracellular staining. Following washing, cells were fixed with 100 µl of fixation buffer and incubated at 4 °C for 30 min protected from light. Permeabilization was then performed by adding 200 µl of 1 × Perm wash buffer and incubating at 4 °C for 30 min or overnight. For intracellular staining, an antibody cocktail containing PerCP-anti human GZMB and PE-anti human IFN-γ was prepared, and 50 µl of the premixed antibodies was added to each sample, followed by incubation at room temperature for 30 min in the dark. The reaction was stopped by adding 150 µl of FCM buffer to each well. Finally, cells were resuspended in 300 µl of 1 × PBS, filtered through a cell strainer, and transferred to flow cytometry tubes for acquisition.

Transwell assay

Cell migration was measured by Transwell assays using the 24-well transwell chambers with 8 µm polycarbonate membranes (Corning Incorporated, USA). For the assay of *GJB2*-regulated tumor cell migration ability, OC cells were collected after transfection with *GJB2* overexpression plasmid or siRNA for 24 h. A total of 2×10^5 cells in 200 µl serum-free medium were added to the upper chamber. The lower chamber contained 800 µl medium with 20% FBS as a chemoattractant. For the assay of *GJB2*'s ability to attract $CD8^+$ T cells, OC cells overexpressing *GJB2* were seeded into the lower chamber. 24 h after transfection, a total of 1×10^6 $CD8^+$ T cells were added to the upper chamber in 200 µl medium containing 10% FBS. At the same time, 800 µl medium containing 10% FBS was added to the lower chamber. After incubation for 24 h, non-migrating cells were removed with a cotton swab, the remaining cells were subsequently fixed with 4% paraformaldehyde for 30 min and stained with crystal violet for 20 min. The relative cell number was calculated a light microscope (Olympus, Tokyo, Japan).

Wound healing assay

After being transfected with *GJB2* siRNA and *GJB2*-OE for 24 h, OC cells were seeded into a 12-well plate and then scraped with a 200 µl pipette tip. Cell migration images were captured at 0, 24, 36, 48, 60, and 72 h after scratching.

Cell counting kit-8 (CCK-8) assay

The influence of *GJB2* siRNA and *GJB2*-OE on cell proliferation was evaluated by CCK-8 assay. Specifically, OC cells (3×10^3 cells/well) were planted into 96-well plates and cultivated at 37 °C for 12, 24, 48, and 72 h, respectively. At different time points, the cells were incubated with the mixture containing 10 µl CCK-8 and 100 µl fresh medium for 2 h at 37 °C. Finally, absorbance was measured at 450 nm with an enzyme-labeled apparatus.

Colony formation assay

A total of 500 cells per well were spread onto six-well plates and cultured at 37 °C for 2 weeks. The fresh medium was changed every three days. Finally, the colonies were treated with 4% paraformaldehyde fixation for 30 min and crystal violet staining for 20 min. Subsequently, a statistical analysis of the colony number was conducted.

Cell viability

Cells were inoculated into 96-well plates at a rate of 3000 cells/well and allowed to attach for 12 h. Elesclomol and copper chloride ($CuCl_2$) solution were added 1:1 for 24 h. Then 100 µl of fresh medium containing 10% CCK8 solution was added and the 450 nm absorbance was detected following incubation for 2 h at 37 °C using an enzyme-labeled apparatus. As for the chemical rescue assay, copper ion chelator (TTM) was added after plating overnight, then Elesclomol-$CuCl_2$ was added into plates and incubated for 24 h.

Western blotting

Cells were cultured in 60 mm dishes to approximately 80% confluence and then lysed with ice-cold lysis RIPA buffer (P0013B) containing 1% protease inhibitor cocktail and the concentration of the supernatant was determined by BCA. After loading the target proteins onto an SDS poly acrylamide gel, the proteins were transferred from the gel to a PVDF membrane. Subsequently, the membranes were incubated at 4 °C overnight with GJB2 (ER1902-42, HUABIO, 1:1000), E-cadherin (20,874–1-AP, Proteintech, 1:2000), N-cadherin (22,018–1-AP, Proteintech, 1:2000), Vimentin (10,366–1-AP, Proteintech, 1:2000) and GAPDH (Utibody, UM4002, 1:2000) after being blocked with 5% BSA for 2 h. After washed 3 times with TBST, the membranes were incubated with a secondary antibody (Zhengneng Biotechnology) for 90 min at room temperature. Protein bands were detected and analyzed using enhanced ECL chemiluminescence. Digital images were taken by a MiniChemi from SageCreation, Beijing, China.

Statistical analyses

For the data comparison between the two groups, we adopted the t-test for variables with a normal distribution and the Wilcoxon rank sum test for variables conforming to non-normal distribution. The overall survival rates of each group were compared using a KM analysis in conjunction with a log-rank test. Additionally, we developed the prognostic signature using the univariate Cox-LASSO-multivariate Cox regression analysis methods. We performed all statistical analyses using the R software (version 4.2.0) and GraphPad Prism software (version 9.0). Statistical significance is indicated with asterisks (*). A two-sided p value of <0.05 was considered statistically significant (*$p<0.05$, **$p<0.01$, ***$p<0.001$, ****$p<0.0001$).

Results

DECGs and molecular characterization in OC patients

To investigate the correlation between cuproptosis-related genes (CRGs) and OC, we compiled a list of 97 cuproptosis genes (CGs) from published articles[23–25], as shown in Table S3. Gene ontology (GO) pathway enrichment analysis of these CGs revealed significant associations with various copper signaling pathways (Fig. 2A). We then compared normal ovarian and OC samples, identifying a total of 5,723 differentially expressed genes (DEGs) ($|Log_2FC|>1$, $p<0.05$; Fig. 2B). Among the 97 CGs, 18 were found to be differentially expressed in the TCGA cohort (Fig. 2B). Of these, 8 DECGs (differentially expressed cuproptosis genes) were upregulated, while 10 were downregulated, indicating dysregulation of cuproptosis in OC (Fig. 2C, Table S5). Further analysis of the expression correlations among the 18 DECGs revealed highly consistent relationships between the regulators of cuproptosis (Fig. 2D).

We next analyzed the somatic mutation frequency of the 18 DECGs and found that 56 out of 462 OC samples (12.12%) harbored mutations in these genes, predominantly in the form of missense mutations (Fig. 2E). We also evaluated somatic copy number variations (CNVs) in the DECGs and observed widespread CNVs across all 18 genes. The frequencies of CNVs in DECGs in OC patients are shown in Fig. 2F, while the chromosomal locations of altered CNVs in these genes are depicted in Fig. 2G. Finally, Pearson correlation analysis revealed significant associations between 1,453 CRGs and the 18 DECGs ($|R|>0.4$, $p<0.001$), as illustrated in the Sankey diagram (Fig. 2H, Table S6). Among these, 71 differential genes were identified within the 1,453 CRGs, including 30 upregulated and 41 downregulated CRGs in tumor tissues ($|Log_2FC|>3$, $p<0.05$; Fig. 2I, Table S7).

Construction and validation of CRGs signature

Univariate Cox regression analysis of 71 CRGs identified 9 CRGs significantly associated with the prognosis of OC patients (Fig. S1A, Table S8). To minimize overfitting during signature generation, we applied LASSO regression analysis, which revealed 7 significant genes and highlighted the trajectory changes in the regression coefficients of mRNAs, as well as estimated prediction accuracy through 1000 cross-validations (Fig. S1B-C). These high-dimensional data were further reduced using a multifactorial Cox proportional hazards regression model, resulting in the selection of 5 CRGs for the development of a risk score model to predict overall survival (OS) in OC patients. The

ID	Description
GO:0005507	copper ion binding
GO:0055076	transition metal ion homeostasis
GO:0006091	generation of precursor metabolites and energy
GO:0010038	response to metal ion
GO:0005759	mitochondrial matrix
GO:0046916	cellular transition metal ion homeostasis
GO:0000041	transition metal ion transport
GO:0006825	copper ion transport
GO:0046688	response to copper ion
GO:0018205	peptidyl-lysine modification

Fig. 2 DECGs and Molecular Characterization in OC Patients. **A** GO pathway enrichment analysis of CGs involved signaling pathway. **B** Venn diagram showing the DECGs shared by TCGA-DEGs and CGs, 18 DECGs were found in the TCGA cohort. **C** Differential expression of 18 DECGs between normal tissue and OC tissues. **D** The correlations between the expression of 18 DECGs. **E** Mutation frequencies of 18 DECGs in 462 patients with OC from the TCGA cohort. **F** Frequency of CNV alterations in 18 DECGs. Red dots represented CNV amplification, while green dots represented CNV deletion. **G** Location of CNV alterations of 18 DECGs on chromosomes in the TCGA-OC cohort. **H** Sankey diagram of coexpression between 18 DECGs and 1453 CRGs. **I** The volcano plot depicted the expression patterns of CRGs in TCGA-OC. *$p<0.05$, **$p<0.01$, ***$p<0.001$, ****$p<0.0001$

selected genes included *CD8B2*, *GJB2*, *GRIP2*, *MELK*, and *PLA2G2D* (Fig. 3A). A heatmap illustrating the relationship between the 18 DECGs and the 5 CRGs is shown in Fig. 3B. Risk score$= (0.39814766790876 * \text{Expression } CD8B2) + (0.319840250099011 * \text{Expression } GJB2) + (11.80464867091524 * \text{Expression } GRIP2) + (-0.652506214718363 * \text{Expression } MELK) + (-0.747117340620353^{*} * \text{Expression } PLA2G2D)$. Based on the median risk score, we classified patients in the TCGA-OC cohort into high-risk and low-risk groups for survival analysis. The KM method was used to compare the OS between the two groups, and the results revealed that the OS of patients in the high-risk group was significantly worse than that of the low-risk group ($p=0.003$, Fig. 3C). Given the strong correlation between the risk model and patient outcomes, we further investigated whether the prognostic value of the 5 CRGs could serve as an independent prognostic factor. In the univariate Cox analysis, both age and risk scores showed statistically significant associations with OS ($p<0.001$, Fig. 3D). Furthermore, in multivariate Cox regression analysis, both variables retained their prognostic significance for OS (Fig. 3E). Subsequently, OC patients were divided into 3 groups (all, training, and testing) to assess the accuracy and feasibility of the prognostic risk model in predicting OC prognosis. The detailed expression levels of the risk genes, risk scores, and risk group assignments are provided in Table S9. The analysis revealed that, in all 3 groups (all, training, and testing), the expression levels of the 5 key risk-scoring genes differed significantly between the high-risk and low-risk groups (Fig. 3F). Specifically, *GRIP2*, *GJB2*, and *CD8B2* were more highly expressed in the high-risk group, whereas *PLA2G2D* and *MELK* had lower expression levels (Fig. 3F). Scatter plots for the 3 groups (all, training, and testing) demonstrated that the mortality rate of OC patients increased with higher risk scores (Fig. 3F).

The receiver operating characteristic (ROC) curve analysis revealed that the area under the curve (AUC) values for evaluating survival outcomes in OC patients at 1, 2, and 3 years were all greater than 0.5, demonstrating the high specificity and sensitivity of the prediction model (Fig. 3G). Three-dimensional principal component analysis (PCA) showed that the distribution of high-risk and low-risk patients was indistinguishable based on the 18 DECGs and all CRGs expression sets (Fig. 3H, I). However, the distribution of high-risk and low-risk groups based on the 5 CRGs was most distinct (Fig. 3J). These results indicate that the 5 CRGs used in the risk model effectively distinguish between high-risk and low-risk samples, further supporting the utility of our method in differentiating these populations. Overall, these findings suggest that the prognostic risk model, based on the 5 genes (*CD8B2*, *GJB2*, *GRIP2*, *MELK*, and *PLA2G2D*), can serve as a reliable predictor of OC prognosis.

Heatmap and KM curves of clinicopathological variables in the high-risk and low-risk groups

To facilitate the clinical application of the prediction model, we integrated clinical data and gene features from TCGA-OC patient samples. We analyzed the association between the CRGs' prognostic signature and clinicopathological characteristics. The heatmap illustrates the distribution of age, grade, stage, and risk score across all OC patient samples (Fig. S2A). The proportions of clinicopathological variables in the high-risk and low-risk groups are shown in Fig. S2B-D. Patients with missing clinical information were excluded from the analysis. We further explored whether prognosis varied across different clinical subgroups by separating samples based on age (≤65 and >65), tumor grade (2 and 3), and stage (III and IV). Survival rates were worse for high-risk patients compared to low-risk patients in all subgroups (Fig. S2E–G). These results suggest that our risk model can accurately predict the prognosis across various clinical subgroups of OC.

Prognostic analysis of the 5 CRGs risk model in TCGA and ICGC cohorts

The prognostic risk score, combined with age and tumor grade, was used to generate the ROC survival curve. The results indicated that, compared to other clinical traits, the CRGs prognostic risk scoring system accurately predicted the 1-, 3-, and 5-year survival rates of OC samples (Fig. 4A–C, AUC = 0.620, 0.593, and 0.601, respectively). Using the 5 CRGs features, we constructed a prognostic nomogram to predict the 1-, 3-, and 5-year OS probabilities. As shown in Fig. 4D, the score assigned to each factor corresponds to its contribution to survival risk. The accuracy of the nomogram was verified using calibration curves, which demonstrated a high degree of agreement between actual values and predicted values (Fig. 4E). Moreover, the C-index for the risk score was greater than 0.5, indicating that the risk model offers a significant advantage in predicting OS in

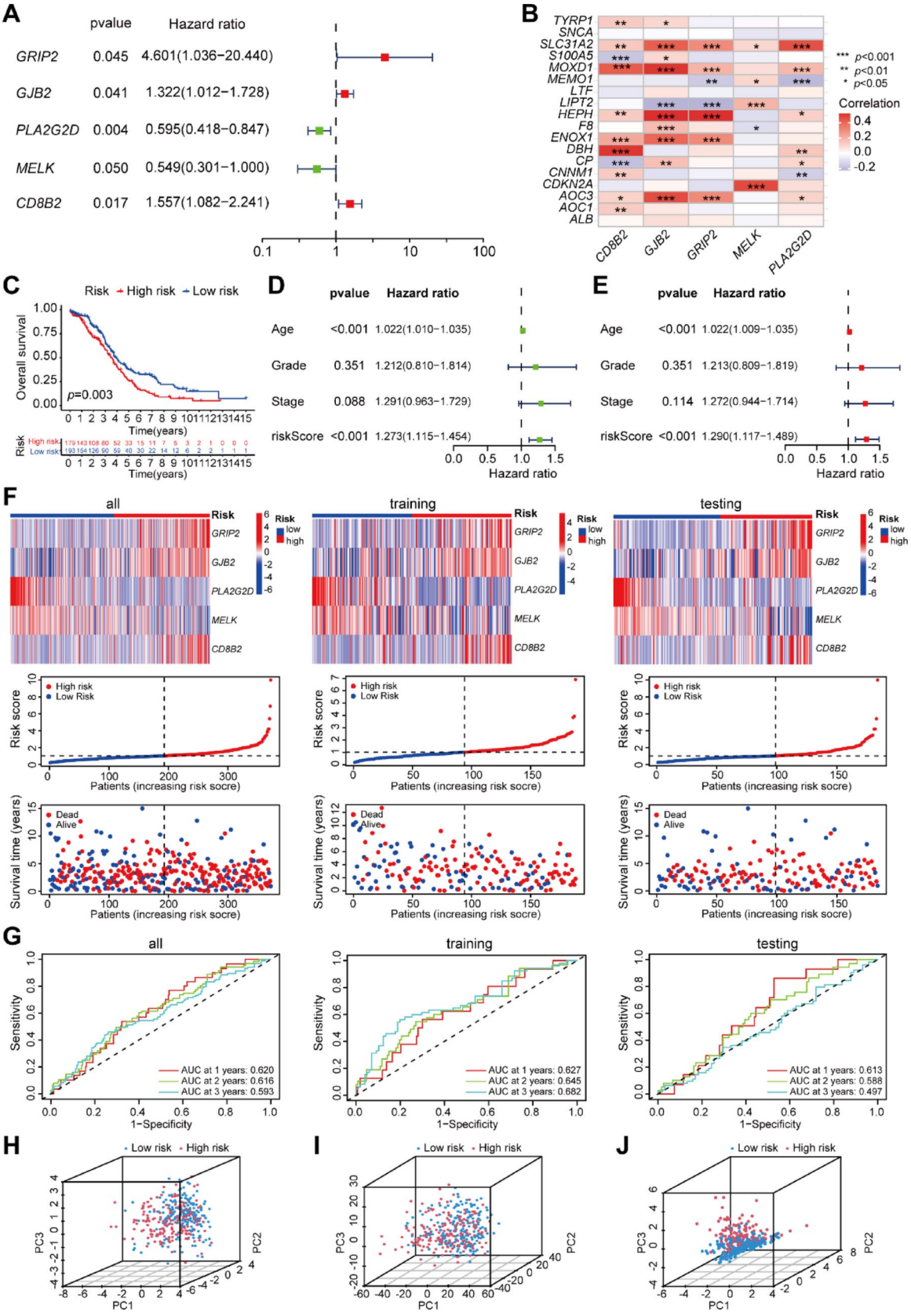
A
pvalue
Hazard ratio
GRIP2 0.045 4.601(1.036−20.440)
GJB2 0.041 1.322(1.012−1.728)
PLA2G2D 0.004 0.595(0.418−0.847)
MELK 0.050 0.549(0.301−1.000)
CD8B2 0.017 1.557(1.082−2.241)
B
TYRP1
SNCA
SLC31A2
S100A5
MOXD1
MEMO1
LTF
LIPT2
HEPH
F8
ENOX1
DBH
CP
CNNM1
CDKN2A
AOC3
AOC1
ALB
CD8B2 GJB2 GRIP2 MELK PLA2G2D
*** p<0.001
** p<0.01
* p<0.05
Correlation
C
Risk High risk Low risk
Overall survival
p=0.003
Time(years)
D
pvalue Hazard ratio
Age <0.001 1.022(1.010−1.035)
Grade 0.351 1.212(0.810−1.814)
Stage 0.088 1.291(0.963−1.729)
riskScore <0.001 1.273(1.115−1.454)
Hazard ratio
E
pvalue Hazard ratio
Age <0.001 1.022(1.009−1.035)
Grade 0.351 1.213(0.809−1.819)
Stage 0.114 1.272(0.944−1.714)
riskScore <0.001 1.290(1.117−1.489)
Hazard ratio
F
all
training
testing
Risk
low
high
GRIP2
GJB2
PLA2G2D
MELK
CD8B2
High risk
Low Risk
Risk score
Patients (increasing risk socre)
Dead
Alive
Survival time (years)
G
all
training
testing
Sensitivity
1−Specificity
AUC at 1 years: 0.620
AUC at 2 years: 0.616
AUC at 3 years: 0.593
AUC at 1 years: 0.627
AUC at 2 years: 0.645
AUC at 3 years: 0.682
AUC at 1 years: 0.613
AUC at 2 years: 0.588
AUC at 3 years: 0.497
H
I
J
Low risk
High risk
PC1
PC2
PC3

Fig. 3 Construction and Validation of CRGs Signature. **A** The forest plot demonstrated the hazard ratio of 5 CRGs with prognostic values filtered by the univariate Cox regression analysis. **B** The heatmap of the correlation between 18 DECGs and 5 CRGs. **C** KM curves for OS of the two risk groups (chi-square test, $p=0.003$). **D** Univariate Cox analysis of the signature with clinical phenotypes. **E** Multivariate Cox regression analysis of the signature with clinical phenotypes. **F** The expression heatmap of 5 CRGs in the 3 groups (all, training, and testing). The ranked dot plot indicates the risk score distribution and the scatter plot presents the patients' survival status. **G** ROC curves to predict the sensitivity and specificity of 1-, 2-, and 3-year survival according to the risk score in the 3 groups (all, training, and testing). (H-J) PCA between the high-risk and low-risk groups based on the 18 DECGs **H**, All CRGs **I**, and 5 CRGs risk model **J**. *$p<0.05$, **$p<0.01$, ***$p<0.001$, ****$p<0.0001$

OC patients (Fig. 4F). To assess the classification ability of the risk model based on the 5 CRGs, we performed PCA (Fig. 4G) and t-distributed stochastic neighbor embedding (t-SNE) (Fig. 4H) on all TCGA datasets. The results showed distinct distributions between the high-risk and low-risk groups, suggesting that the prognostic signature accurately differentiates between them (Fig. 4G, H). Additionally, when we compared our CRGs signature prognostic model with the Tumor Immune Dysfunction and Exclusion (TIDE) model and the Tumor Inflammation Signature (TIS) model, we found that our model had a superior ability to predict the 1-year survival rate of OC samples (Fig. 4I, AUC = 0.620, 0.579, and 0.497, respectively).

In the ICGC cohorts, patients with OC were also divided into high-risk and low-risk groups. KM curves revealed that patients in the low-risk group had a significantly better survival benefit (Fig. 4J). Additionally, the AUC values for 1-, 2-, and 3-year survival in the ICGC cohorts were 0.645, 0.708, and 0.691, respectively (Fig. 4K). The scatter plot further demonstrated that patients in the low-risk group exhibited more favorable prognostic outcomes (Fig. 4L, M). Finally, PCA and t-SNE analyses of the ICGC data sets revealed a clear distinction between high-risk and low-risk components, indicating that the prognostic signature accurately differentiated the two groups (Fig. 4N, O). These results collectively demonstrate that the gene signature performs well in predicting the prognosis of patients in both groups.

Risk score of CRGs predicts the signaling pathways, tumor microenvironment, and immune cell infiltration

We conducted GSEA using both KEGG and GO databases to investigate the differences in biological functions and signaling pathways between the high-risk and low-risk groups defined by the 5 CRG signatures (Fig. 5A, B, Fig. S3A-B). The high-risk group exhibited significant enrichment in pathways such as ECM receptor interaction, focal adhesion, and WNT signaling, while the low-risk group was notably enriched in pathways related to chemokine signaling and primary immunodeficiency (Fig. 5A, B). We also analyzed the immune microenvironment of samples with different risk scores and obtained their immune expression profiles (Fig. S4A). Additionally, GSVA enrichment analysis revealed significant differences between the high-risk and low-risk groups in several immune-related pathways, including Type II IFN response, MHC class I, *HLA*, cytolytic activity, inflammation promotion, T cell co-stimulation, checkpoint regulation, T cell co-inhibition, and APC co-inhibition (Fig. S4B, Table S10).

We next used CIBERSORT to compare immune cell infiltration between the high-risk and low-risk groups. In the low-risk group, we observed a higher proportion of memory B cells, plasma cells, $CD8^+$ T cells, activated memory $CD4^+$ T cells, follicular helper T cells, activated NK cells, and M1 macrophages. In contrast, the high-risk group had a lower proportion of naive B cells, resting memory $CD4^+$ T cells, monocytes, and activated mast cells (Fig. 5C). Since human leukocyte antigen (*HLA*) genes are critical for antigen presentation, we analyzed *HLA* indexes that are closely associated with immune function. Our analysis revealed a significant upregulation of *HLA* gene expression in the low-risk group compared to the high-risk group, encompassing both classical class I (*HLA-A*) and class II molecules (*HLA-DQA1*, *HLA-DOB*, *HLA-DMB*), as well as the non-classical *HLA-F* (Fig. S4C). This elevated *HLA* expression profile suggests enhanced antigen presentation capacity in low-risk patients, which is generally associated with more robust anti-tumor immune responses. Additionally, we examined the expression of m6A-related genes in the high-risk and low-risk groups. The results showed that only *FTO* expression differed significantly, with higher expression in the high-risk group compared to the low-risk group (Fig. S4D).

To further evaluate the predictive value of risk scores for immunotherapy, we evaluated immune scores in OC cells using the ESTIMATE algorithm and found that the low-risk group had higher immune scores (Fig. 5D), indicating a more immunologically active tumor microenvironment. Importantly, our analysis of immune exclusion patterns demonstrated a significant positive association with risk scores (Fig. 5E), suggesting that tumors from high-risk patients exhibit characteristics of immunologically "cold" tumors that are less responsive to immune checkpoint blockade (ICI) therapy. Previous studies have shown that Tumor Mutation Burden (TMB) is positively correlated with tumor stage, grade, and immune cell infiltration [37]. We categorized OC patients into "high-TMB" and "low-TMB" groups using median cutoff points and performed survival analyses. Kaplan–Meier analysis revealed that patients in the high-TMB group had significantly better OS compared to those

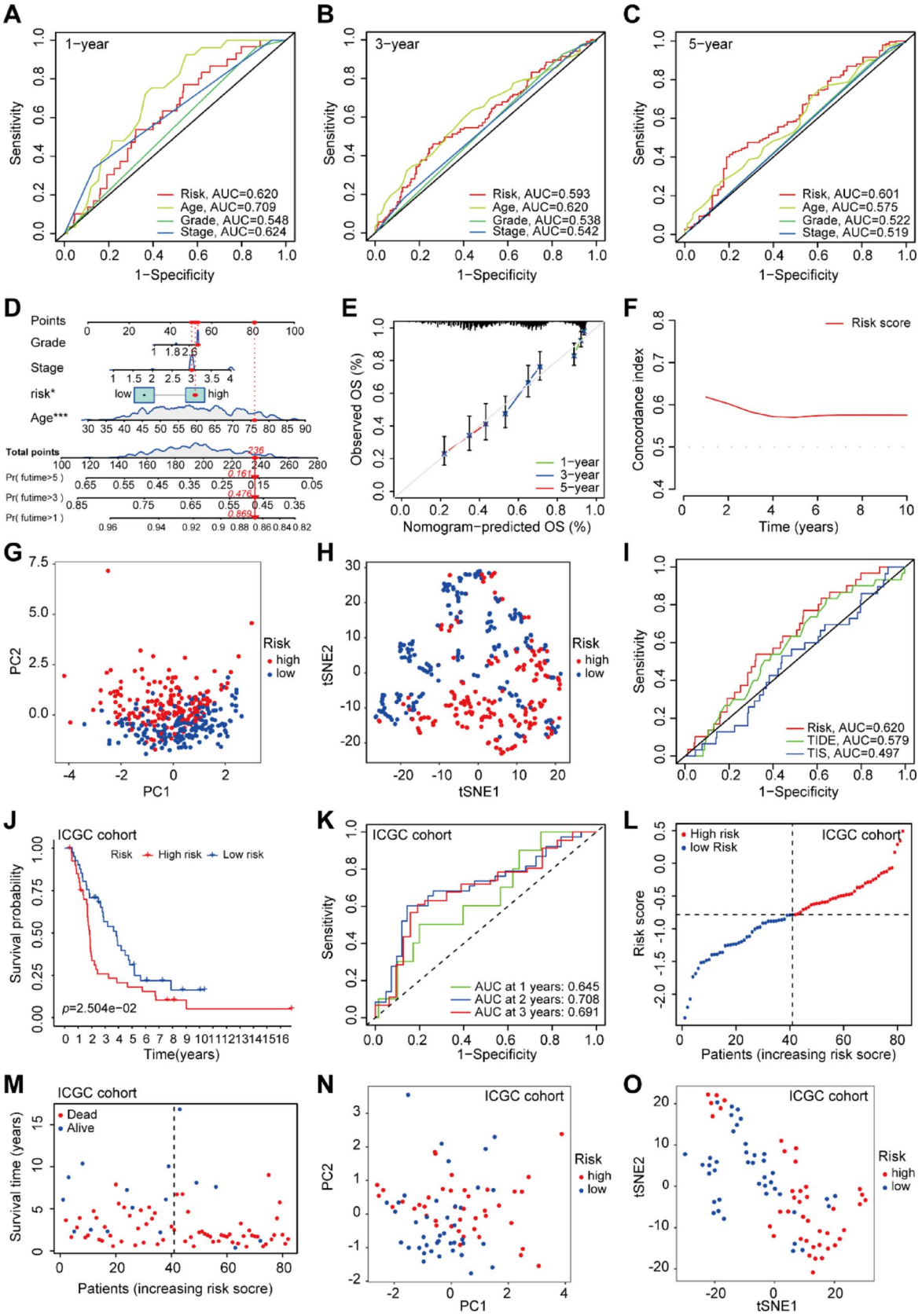
A
1−year
Sensitivity
1−Specificity
Risk, AUC=0.620
Age, AUC=0.709
Grade, AUC=0.548
Stage, AUC=0.624
B
3−year
Sensitivity
1−Specificity
Risk, AUC=0.593
Age, AUC=0.620
Grade, AUC=0.538
Stage, AUC=0.542
C
5−year
Sensitivity
1−Specificity
Risk, AUC=0.601
Age, AUC=0.575
Grade, AUC=0.522
Stage, AUC=0.519
D
Points
Grade
Stage
risk*
low
high
Age***
Total points
Pr(futime>5)
Pr(futime>3)
Pr(futime>1)
E
Observed OS (%)
Nomogram−predicted OS (%)
1−year
3−year
5−year
F
Risk score
Concordance index
Time (years)
G
PC2
PC1
Risk
high
low
H
tSNE2
tSNE1
Risk
high
low
I
Sensitivity
1−Specificity
Risk, AUC=0.620
TIDE, AUC=0.579
TIS, AUC=0.497
J
ICGC cohort
Risk
High risk
Low risk
Survival probability
p=2.504e−02
Time(years)
K
ICGC cohort
Sensitivity
1−Specificity
AUC at 1 years: 0.645
AUC at 2 years: 0.708
AUC at 3 years: 0.691
L
High risk
low Risk
ICGC cohort
Risk score
Patients (increasing risk socre)
M
ICGC cohort
Dead
Alive
Survival time (years)
Patients (increasing risk socre)
N
ICGC cohort
PC2
PC1
Risk
high
low
O
ICGC cohort
tSNE2
tSNE1
Risk
high
low

Fig. 4 Prognostic Analysis of the 5 CRGs Risk Model in TCGA and ICGC Cohorts. **A**–**C** ROC curve of 1-, 3-, and 5-year OS for multiple prognostic indicators of OC samples. **D** The nomogram, a quantitative model for predicting clinical prognosis, to predict 1-year, 3-year, and 5-year OS in the OC patients of the TCGA-OC cohort using 3 factors, including Age, Grade, and risk score. **E** The calibration curves indicated that the nomogram accurately predicted the 1-, 3-, and 5-year OS of OC patients in the TCGA cohort. **F** A concordance index (C-index) was generated to assess the identification and forecasting capabilities of the nomogram. **G** The PCA analysis based on the prognostic signature demonstrated that the patients in the different risk score groups were distributed in two directions. Red and blue dots represent the high-risk group and the low-risk group. **H** t-SNE analysis of risk groups in all TCGA cohorts. **I** Comparison of the prognostic risk model with TIS models and TIDE models. TIS: Tumor Inflammation Signature; TIDE: Tumor Immune Dysfunction and Exclusion. **J** KM survival analysis of high and low-risk groups in ICGC cohorts. **K** 1-, 2-, and 3-year ROC curve analysis in ICGC cohorts. **L** The distribution of the risk score in the ICGC cohorts. **M** The correlation of survival time and risk scores in ICGC cohorts. **N** PCA between low-risk and high-risk groups in ICGC cohorts. **O** t-SNE analysis of risk groups in the ICGC cohorts. *$p<0.05$, **$p<0.01$, ***$p<0.001$, ****$p<0.0001$

in the low-TMB group ($p<0.001$, Fig. 5F). A combined survival analysis of TMB and CRG risk scores further revealed that patients with both high TMB and low-risk scores had the best prognosis, while those with low TMB and high-risk scores had the worst prognosis (Fig. 5G). We conclude that patients in the low-risk group are more likely to benefit from immunotherapy.

Immunotherapy analysis and drug sensitivity prediction in high-risk and low-risk groups

Several studies have shown that combination therapy with anti-CTLA-4 and anti-PD-1 can increase the proportion of activated $CD8^+$ T cells and NK cells while reducing the number of suppressive immune cells in the tumor microenvironment, thereby enhancing the therapeutic efficacy against cancer [38, 39]. Building on this background and our analysis of immune checkpoints, we sought to investigate whether there are differences in immunotherapy response between high-risk and low-risk groups. To do so, we downloaded the OC immunotherapy score data from The Cancer Immunome Atlas (TCIA, https://tcia.at/) and assessed the correlation of immunotherapy response between the two risk groups. The results indicated that patients in the low-risk group had a better response to immunotherapy, whether treated with anti-CTLA-4 and anti-PD-1 alone or in combination (Fig. 6A–D). This finding further supports our hypothesis that the risk score can predict the sensitivity and efficacy of immunotherapy.

Chemotherapy resistance remains a significant challenge in the treatment of OC and contributes substantially to cancer-related mortality. Identifying the chemotherapy-sensitive population could optimize the therapeutic efficacy for OC patients, maximizing the benefits of standard chemotherapy protocols. To further investigate the drug resistance potential between high-risk and low-risk groups, we used the "pRRophetic" package to estimate the IC50 values of chemotherapy drugs and inhibitors for both groups. 6 representative drugs are shown in Fig. 6E-F. Our analysis identified Ruxolitinib, Temozolomide, and Tubastatin A as potential candidates for treating patients in the low-risk group, while Trametinib, Midostaurin, and 17-AAG (Tanespimycin) may offer therapeutic benefits for patients in the high-risk group.

Analysis of *GJB2* expression and survival prognosis in OC

To further validate the prognostic signature, we conducted functional assays through in vitro experiments. Among these 5 signature genes (*CD8B2*, *GJB2*, *GRIP2*, *MELK*, and *PLA2G2D*), *GJB2* was associated with the largest number of cuproptosis genes (Table S6) and exhibited strong positive correlations with multiple key tumor-related signaling pathways (Fig. 7A). A literature review showed that *GJB2* has not been previously reported in OC, prompting us to include *GJB2* for further functional and mechanistic analysis in this study. First, we assessed *GJB2* expression in normal ovarian surface epithelial cells (IOSE) and OC cell lines (HO 8910, A2780, OC314, and SKOV3). The qPCR results indicated that *GJB2* expression was significantly higher in OC cell lines compared to IOSE cells (Fig. 7B). Subsequently, we analyzed clinical specimens from 42 OC patients and 16 normal ovarian controls obtained from Xiangya Hospital, Central South University. qPCR analysis demonstrated significantly elevated *GJB2* expression levels in tumor tissues compared to normal ovarian tissues (Fig. 7C). Additionally, we analyzed GJB2 protein expression patterns in OC through immunohistochemical data from the Human Protein Atlas (HPA, https://www.proteinatlas.org/) database. The IHC results consistently demonstrated upregulated GJB2 protein expression in OC tissues compared to normal ovarian tissue (Fig. 7D), corroborating our qPCR-based observations and further supporting the potential oncogenic role of *GJB2* in OC development.

Through comprehensive bioinformatic analysis of multiple independent cohorts, we consistently observed significant upregulation of *GJB2* expression in OC tissues versus normal controls, as evidenced by data from the TCGA+GTEx (Fig. 7E), GSE38666 (Fig. 7F), and GSE105437 (Fig. 7G). Additionally, we assessed the diagnostic performance of *GJB2* using the area under the ROC curve (AUC) in the TCGA (Fig. 7H), GSE38666 (Fig. 7I), and GSE105437 (Fig. 7J) datasets. The AUC values were 0.954, 0.744, and 0.918, respectively, indicating that *GJB2* has strong diagnostic value in OC patients. Importantly,

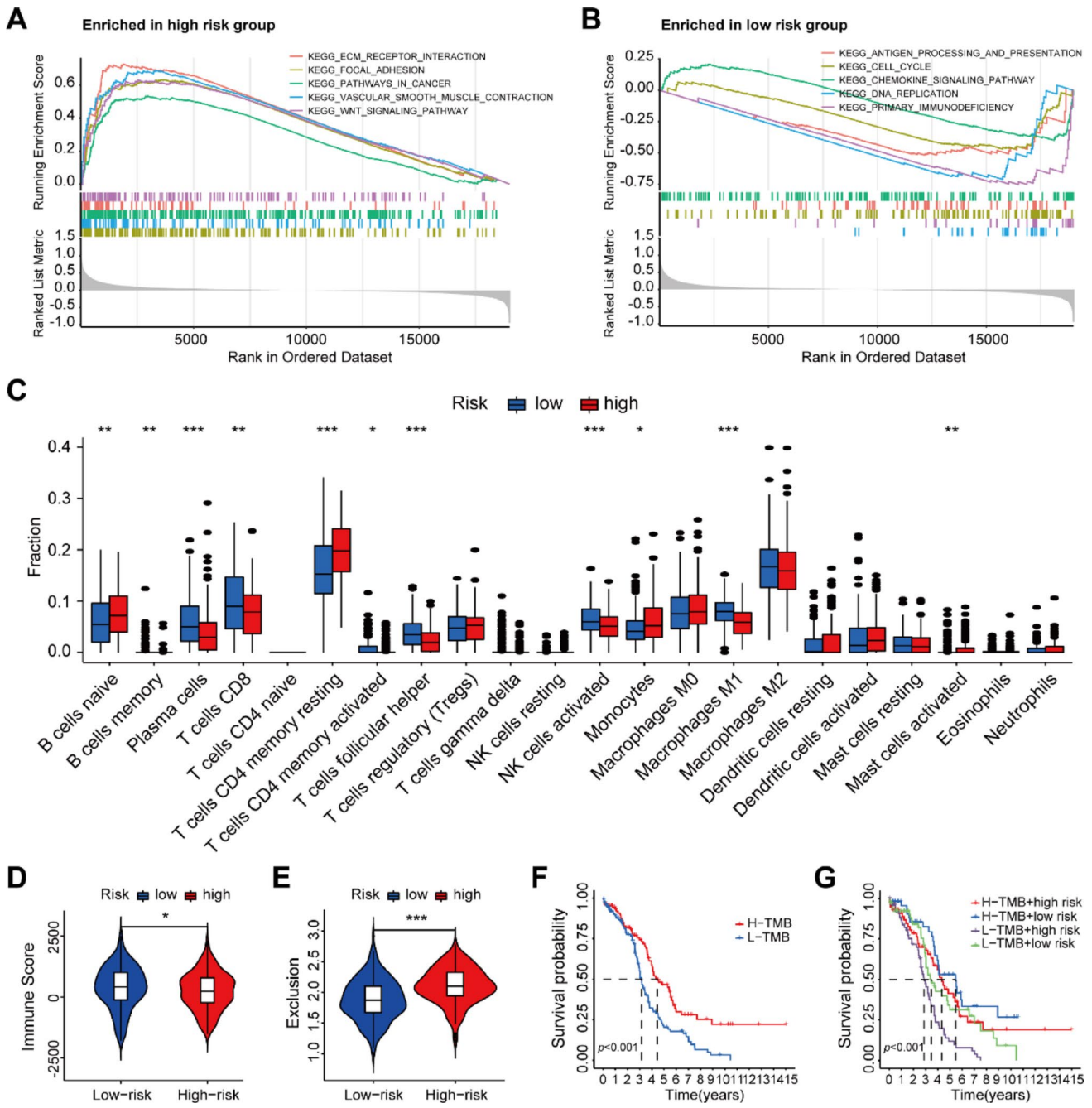

Fig. 5 Risk Score of CRGs Predicts the Signaling Pathways, Tumor Microenvironment, and Immune Cell Infiltration. (A-B) GSEA enrichment analysis (KEGG) between the high-risk **A** and low-risk **B** groups. **C** The abundance of infiltrating immune cell types in the high-risk and low-risk groups. **D** Comparison of immune-related scores between the high-risk and low-risk groups. **E** Violin plot illuminating the difference in the exclusion score between the high-risk and low-risk groups. **F** Survival analysis curves of the high-TMB and low-TMB groups. **G** Effect of TMB with different risks on the probability of survival. *$p<0.05$, **$p<0.01$, ***$p<0.001$, ****$p<0.0001$

analysis using the KM Plotter website (https://kmplot.com/analysis/) revealed that high expression of *GJB2* was associated with poorer OS outcomes in the TCGA-OC dataset (Fig. 7K). In addition to OS, high expression of *GJB2* was also linked to worse progression-free survival (PFS) outcomes (Fig. 7L). Similarly, the GEPIA2 website (http://gepia2.cancer-pku.cn/#index) revealed that *GJB2* expression increases with the advancing OC stage (Fig. 7M). To further investigate the relationship between *GJB2* expression and OC prognosis, we evaluated its prognostic significance in the GEO dataset cohort (GSE63885). Meta-analysis confirmed that *GJB2* is an independent prognostic factor, with high expression associated with poor prognosis in OC patients (Fig. 7N). Additionally, we assessed the diagnostic

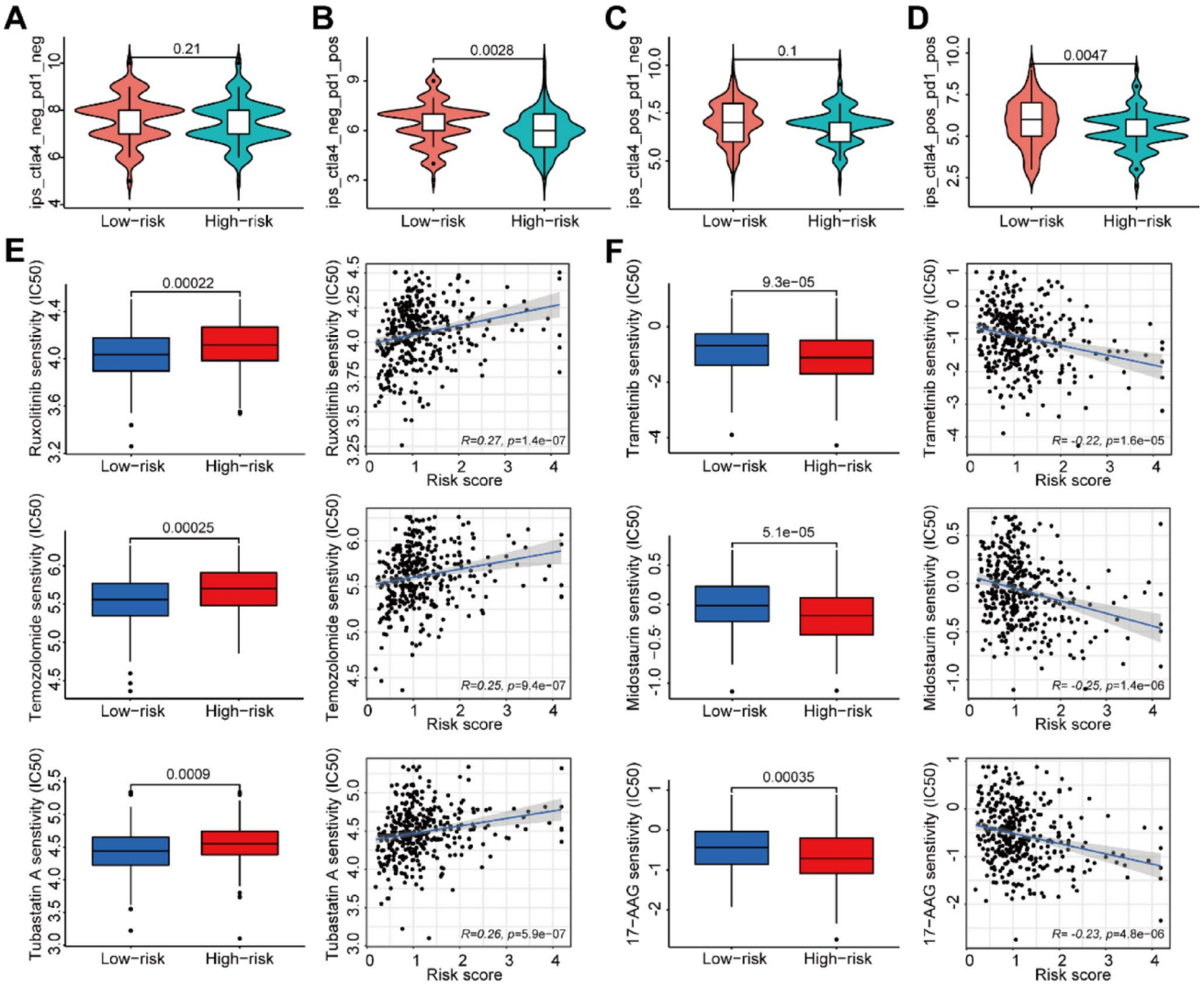

Fig. 6 Immunotherapy Analysis and Drug Sensitivity Prediction in High-risk and Low-risk Groups. **A**–**D** Differences in sensitivity to anti-PD-1, anti-CTLA-4, and the combination of these two antibodies in different risk score groups. **E**, **F** Boxplot showing the mean differences in estimated IC50 values of 6 representative drugs (Ruxolitinib, Temozolomide, Tubastatin A, Trametinib, Midostaurin, and 17-AAG) between the two risk groups

utility of *GJB2* to differentiate between tumor and normal samples in the GSE63885 cohort using ROC analysis. The ROC curve showed that the AUC values for predicting patient survival at 1-, 3-, and 5-years were all greater than 0.5 (Fig. 7O). These findings from independent validation cohorts collectively demonstrate that *GJB2* holds significant diagnostic and prognostic value for OC patients.

Subsequently, we investigated the relationship between *GJB2* expression and the response to anti-tumor drugs. Gene Set Cancer Analysis (GSCA, http://bioinfo.life.hust.edu.cn/GSCA/#/) indicated a significant correlation between *GJB2* expression and drug sensitivity. The results revealed that *GJB2* expression was negatively associated with the sensitivity to several chemotherapeutic agents, including Afatinib, Cetuximab, Docetaxel, Gefitinib, and Trametinib (Fig. 7P). To further explore potential therapeutic options, we used the "prophetic" R package to estimate the IC50 values of various chemotherapy agents and inhibitors in groups with high and low *GJB2* expression. 8 representative drugs are shown in Fig. S5. The analysis showed that the high *GJB2* expression group exhibited greater sensitivity to Paclitaxel, MG-132, Sunitinib, Lapatinib, Dasatinib, Pazopanib, Cyclopamine, and Crizotinib. These findings suggest that OC patients with high *GJB2* expression may benefit from treatment with these drugs. Therefore, *GJB2* expression could serve as a predictor of chemotherapy sensitivity, enabling the estimation of chemotherapy responses based on *GJB2* expression levels in OC patients.

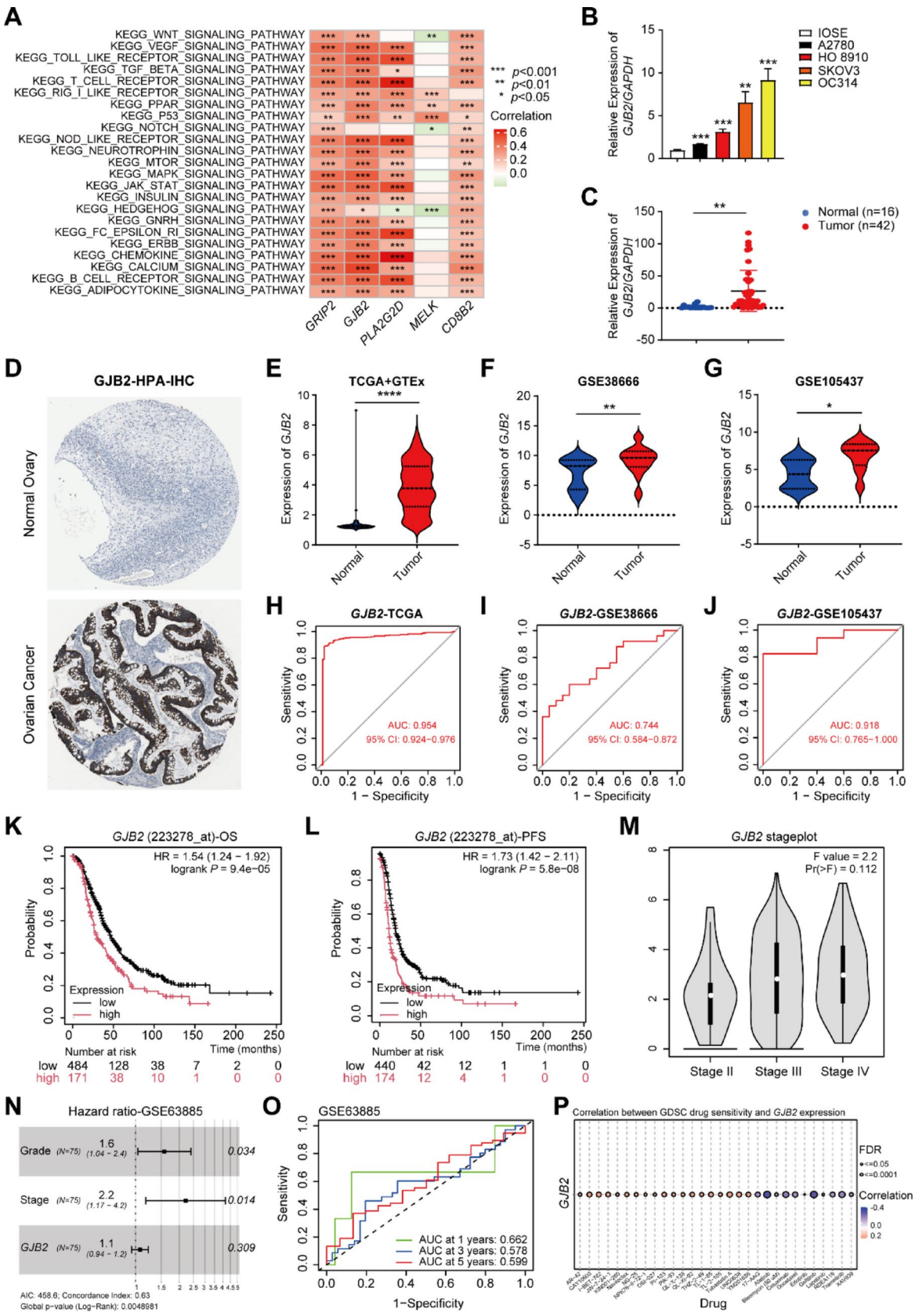
A
KEGG_WNT_SIGNALING_PATHWAY
KEGG_VEGF_SIGNALING_PATHWAY
KEGG_TOLL_LIKE_RECEPTOR_SIGNALING_PATHWAY
KEGG_TGF_BETA_SIGNALING_PATHWAY
KEGG_T_CELL_RECEPTOR_SIGNALING_PATHWAY
KEGG_RIG_I_LIKE_RECEPTOR_SIGNALING_PATHWAY
KEGG_PPAR_SIGNALING_PATHWAY
KEGG_P53_SIGNALING_PATHWAY
KEGG_NOTCH_SIGNALING_PATHWAY
KEGG_NOD_LIKE_RECEPTOR_SIGNALING_PATHWAY
KEGG_NEUROTROPHIN_SIGNALING_PATHWAY
KEGG_MTOR_SIGNALING_PATHWAY
KEGG_MAPK_SIGNALING_PATHWAY
KEGG_JAK_STAT_SIGNALING_PATHWAY
KEGG_INSULIN_SIGNALING_PATHWAY
KEGG_HEDGEHOG_SIGNALING_PATHWAY
KEGG_GNRH_SIGNALING_PATHWAY
KEGG_FC_EPSILON_RI_SIGNALING_PATHWAY
KEGG_ERBB_SIGNALING_PATHWAY
KEGG_CHEMOKINE_SIGNALING_PATHWAY
KEGG_CALCIUM_SIGNALING_PATHWAY
KEGG_B_CELL_RECEPTOR_SIGNALING_PATHWAY
KEGG_ADIPOCYTOKINE_SIGNALING_PATHWAY
GRIP2
GJB2
PLA2G2D
MELK
CD8B2
*** p<0.001
** p<0.01
* p<0.05
Correlation
0.6
0.4
0.2
0.0
B
Relative Expression of GJB2/GAPDH
IOSE
A2780
HO 8910
SKOV3
OC314
C
Relative Expression of GJB2/GAPDH
Normal (n=16)
Tumor (n=42)
D
GJB2-HPA-IHC
Normal Ovary
Ovarian Cancer
E
TCGA+GTEx
Expression of GJB2
Normal
Tumor
F
GSE38666
G
GSE105437
H
GJB2-TCGA
Sensitivity
1 − Specificity
AUC: 0.954
95% CI: 0.924−0.976
I
GJB2-GSE38666
AUC: 0.744
95% CI: 0.584−0.872
J
GJB2-GSE105437
AUC: 0.918
95% CI: 0.765−1.000
K
GJB2 (223278_at)-OS
HR = 1.54 (1.24 − 1.92)
logrank P = 9.4e−05
Probability
Expression
low
high
Time (months)
Number at risk
low 484 128 38 7 2 0
high 171 38 10 1 0 0
L
GJB2 (223278_at)-PFS
HR = 1.73 (1.42 − 2.11)
logrank P = 5.8e−08
low 440 42 12 1 1 0
high 174 12 4 1 0 0
M
GJB2 stageplot
F value = 2.2
Pr(>F) = 0.112
Stage II
Stage III
Stage IV
N
Hazard ratio-GSE63885
Grade (N=75) 1.6 (1.04 − 2.4) 0.034
Stage (N=75) 2.2 (1.17 − 4.2) 0.014
GJB2 (N=75) 1.1 (0.94 − 1.2) 0.309
AIC: 458.6; Concordance Index: 0.63
Global p−value (Log−Rank): 0.0048981
O
GSE63885
AUC at 1 years: 0.662
AUC at 3 years: 0.578
AUC at 5 years: 0.599
1−Specificity
P
Correlation between GDSC drug sensitivity and GJB2 expression
GJB2
FDR
<=0.05
<=0.0001
Correlation
Drug

Fig. 7 Analysis of *GJB2* Expression and Survival Prognosis in OC. **A** GSVA analyzed the signaling pathways involved in 5 characteristic genes (*CD8B2*, *GJB2*, *GRIP2*, *MELK*, and *PLA2G2D*). **B** The expression of *GJB2* in normal ovarian surface epithelial cells (IOSE) and OC cell lines (HO 8910, A2780, OC314, and SKOV3) were detected by qPCR. **C***GJB2* expression levels in OC and normal ovarian tissues were quantified by qPCR. **D** Representative IHC staining for GJB2 protein in normal ovarian tissue and OC tissue, taken from the HPA with permission on its website. **E**–**G** The violin plot depicts the upregulation of *GJB2* in OC tumor samples in TCGA+GTEx, GSE38666, and GSE105437. **H**–**J** ROC Curves Displaying the Sensitivity and Specificity of *GJB2* for the Diagnosis of OC Patients from the TCGA, GSE38666, and GSE105437 Dataset. **K** KM survival curves for OS in OC patients according to the tumor expression of *GJB2*. **L** KM survival curves for PFS in OC patients according to the tumor expression of *GJB2*. **M** GEPIA2 online website analysis showed a correlation between *GJB2* and the OC stage. **N** Meta-analysis depicting forest plots of *GJB2* expression in GSE63885 datasets as a univariate predictor of OS. **O** ROC curves display the sensitivity and specificity of *GJB2* for the diagnosis of OC patients from the GSE63885 datasets. X-axis indicates false-positive rates, and Y-axis indicates true-positive rates. **P** Correlation between *GJB2* expression and the sensitivity of GDSC drugs (top 30). Positive correlation indicates a higher gene expression may lead to drug resistance. Negative correlation indicates a higher gene expression may make drug-sensitive. In all statistical plots, data are expressed as the mean±SD. *$p<0.05$, **$p<0.01$, ***$p<0.001$, ****$p<0.0001$

GJB2 modulates malignant phenotypes and EMT in OC cells

In this study, SKOV3 and OC314 cells exhibited higher expression levels of *GJB2* compared to A7820 and HO 8910 cells (Fig. 7B). To further investigate the role of *GJB2*, we selectively knocked down *GJB2* in SKOV3 and OC314 cells using siRNA. The siRNA constructs *GJB2*-si2 and *GJB2*-si3 were chosen for subsequent assays due to their effective knockdown efficiency (Fig. 8A, S6A). To assess the impact of *GJB2* knockdown on cell proliferation, we performed CCK-8 (Fig. 8B, S6B) and colony formation (Fig. 8C, S6C) assays in SKOV3/OC314 cells with or without *GJB2* knockdown. The results showed that, following *GJB2* knockdown, the proliferation rate in the *GJB2*-si2 and *GJB2*-si3 groups was significantly reduced compared to the siNC control group (Fig. 8B-C, S6B-C). We also examined the effect of *GJB2* knockdown on cell migration using Transwell (Fig. 8D, S6D) and wound healing (Fig. 8E, S6E) assays. Both assays revealed a marked reduction in the migratory ability of OC cells upon inhibition of *GJB2* expression. Collectively, these findings suggest that silencing *GJB2* expression inhibits both the proliferation and migration of OC cells.

We further investigated the potential effects of *GJB2* upregulation on OC cells. *GJB2* overexpression (*GJB2*-OE) plasmids were constructed and transfected into HO 8910 and A2780 cells, followed by the detection of *GJB2* overexpression using qPCR and Western blotting assays. The results showed that *GJB2* was markedly elevated in both HO 8910 and A2780 cells (Fig. 8F, S6F). In both CCK-8 (Fig. 8G, S6G) and colony formation (Fig. 8H, S6H) assays, *GJB2*-OE promoted OC cell proliferation. Additionally, in comparison to the control group, *GJB2*-OE significantly increased the relative migration rate of OC cells in both Transwell (Fig. 8I, S6I) and wound healing (Fig. 8J, S6J) assays. These findings suggest that targeting *GJB2* could offer potential therapeutic strategies for treating OC.

After determining *GJB2*'s critical role in regulating the malignant progression of OC, we next investigated its potential involvement in EMT. Bioinformatics analysis using the GSCA platform (Gene Set Cancer Analysis, http://bioinfo.life.hust.edu.cn/GSCA/#/) revealed significant enrichment of EMT-related pathways in OC samples with high *GJB2* expression (Fig. 8K). To validate these findings experimentally, we examined EMT marker expression in *GJB2*-overexpressing OC cells. Both qPCR (Fig. 8L) and Western blotting (Fig. 8M) analyses demonstrated that *GJB2* overexpression significantly downregulated the epithelial marker E-cadherin while upregulating the mesenchymal markers N-cadherin and Vimentin. These results suggest that *GJB2* may promote OC metastasis by activating the EMT processes.

GJB2 is associated with copper ionophore-induced cell death

Building upon our investigation of *GJB2*'s functional roles, we further examined its potential involvement in cuproptosis regulation. GO enrichment analysis of *GJB2*-correlated genes ($|R|>0.45$, $p<0.001$, Table S11) revealed significant enrichment in copper ion binding pathways (GO:0005507, $p=2.4\times10^{-4}$, Fig. 9A), suggesting *GJB2* may modulate cuproptosis through copper-related processes. Subsequent qPCR analysis revealed that overexpression of *GJB2* in OC cells led to significant downregulation of key cuproptosis regulators (*FDX1*, *DLAT*, *LIAS*, and *PDHB*) (Fig. 9B). These findings collectively indicate that *GJB2* participates in cuproptosis regulation by modulating the expression of core pathway components.

Accumulating evidence suggests that Elesclomol is a copper-binding small molecule and Elesclomol-induced cell death results from the accumulation of intracellular copper rather than from the direct effects of Elesclomol itself [40, 41]. However, the mechanisms underlying copper-induced cytotoxicity in OC cells remain unclear. To investigate this, we first assessed the IC50 values of HO 8910 and A2780 cells treated with Elesclomol-$CuCl_2$ (1:1) for 24 h. The IC50 values were found to be 30 nM and 15 nM, respectively (Fig. 9C, D). We then constructed a cuproptosis induction model, which included 3 experimental groups: negative control (NC), Elesclomol-$CuCl_2$, and TTM-Elesclomol-$CuCl_2$.

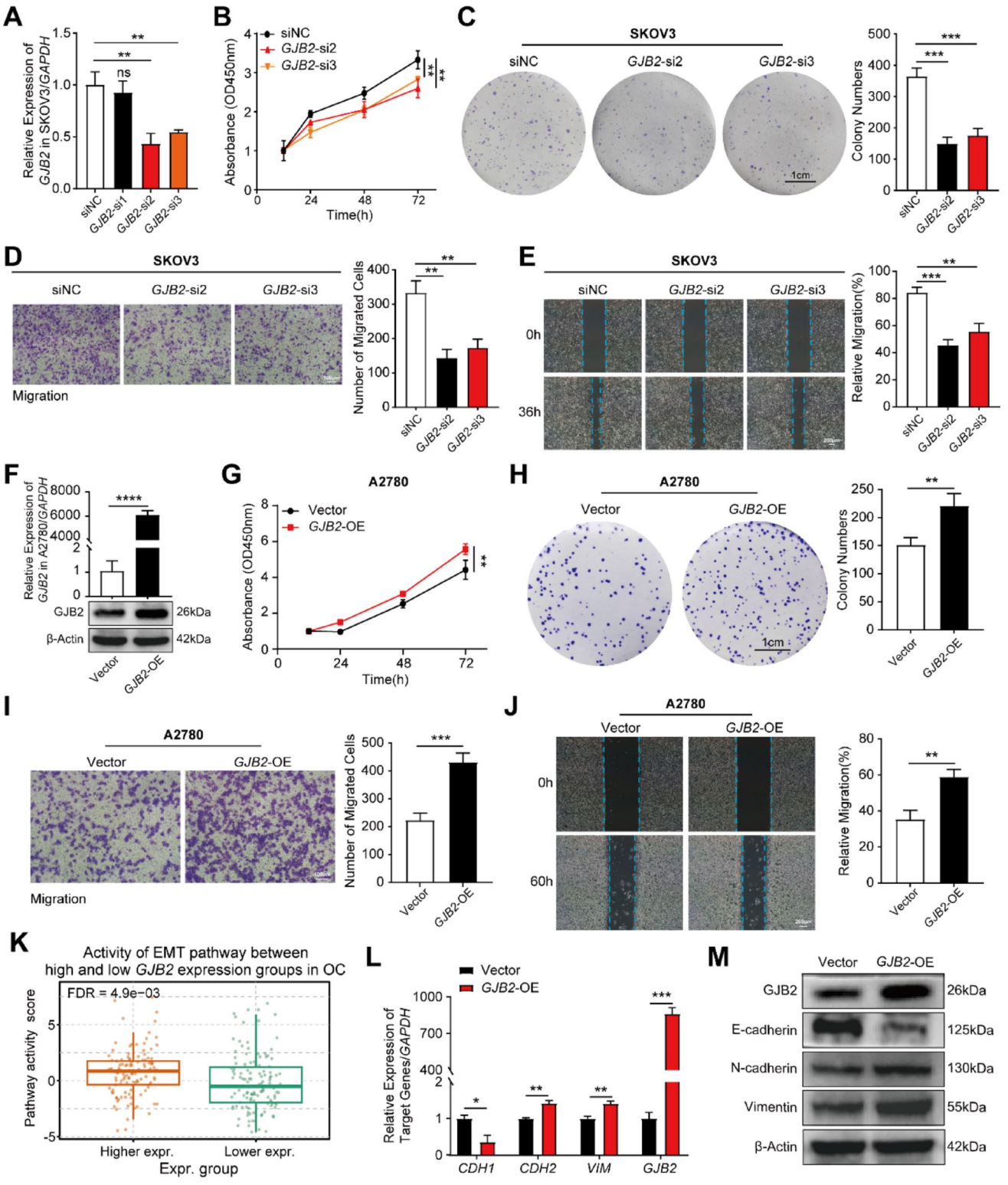

In the Elesclomol-$CuCl_2$ group, HO 8910 cells were treated with 30 nM Elesclomol-$CuCl_2$ (1:1, Elesclomol is a potent copper ionophore which induces cuproptosis) for 24 h. In the TTM-Elesclomol-$CuCl_2$ group, HO 8910 cells were pretreated overnight with 20 μM tetrathiomolybdate (TTM, a copper ion chelator that inhibits cuproptosis), and then treated with 30 nM Elesclomol-$CuCl_2$ for 24 h. The results showed that TTM rescued the viability of HO 8910 cells under Elesclomol-$CuCl_2$-induced conditions (Fig. 9E, F). Similar results were observed in another OC cell line A2780

Fig. 8 *GJB2* Modulates Malignant Phenotypes and EMT in OC Cells. **A** The transfection efficiency of *GJB2* siRNA in SKOV3 was detected by qPCR. **B** The CCK-8 assay showed that *GJB2* interference significantly inhibited SKOV3 cell proliferation at 12, 24, 48, and 72 h. **C** Knockdown of *GJB2* inhibited the proliferation ability of SKOV3 cells and was evaluated by a colony formation assay. **D**–**E** Transwell (**D**) and wound healing (**E**) assays were performed to determine the effect of *GJB2* knockdown on the migration ability of SKOV3 cells. **F** Validation of *GJB2* expression after transfection of *GJB2*-OE and negative control (NC) plasmids in A2780 cells using qPCR and Western blotting assays. **G** CCK-8 assay displaying the influence of *GJB2*-OE on the cell viability. **H** The colony formation assay displays the effect of *GJB2* upregulation on cell proliferation ability. **I**–**J** The effects of *GJB2*-OE on OC cell migration were evaluated through Transwell (**I**) and wound healing (**J**) assays. **K** Bioinformatic analysis of *GJB2*-associated signaling pathways in OC using GSCA. **L**–**M** The mRNA and protein levels of GJB2, E-cadherin, N-cadherin, and Vimentin in A2780 cells after *GJB2* overexpression were detected by qPCR (**L**) and Western blotting (**M**). In all statistical plots, data are expressed as the mean ± SD. *$p<0.05$, **$p<0.01$, ***$p<0.001$, ****$p<0.0001$

(Fig. 9E, F). These findings collectively suggest that Elesclomol-induced OC cell death is dependent on copper accumulation. To further elucidate the role of copper in OC cells and clarify the function of *GJB2* in cuproptosis, we assessed the recovery of OC cell viability in the Vector and *GJB2*-OE groups following treatment with Elesclomol-$CuCl_2$. Both groups were treated with varying concentrations of Elesclomol-$CuCl_2$ for 24 h, and cell viability was measured using the CCK-8 assay. The results indicated that *GJB2*-OE significantly increased the IC50 value (Fig. 9G, H). Additionally, the bar chart revealed a significant difference in cell viability between the two groups after 24 h of Elesclomol-$CuCl_2$ treatment, with the *GJB2*-OE group showing markedly higher viability than the Vector group (Fig. 9I, J). This suggests that *GJB2* overexpression enables OC cells to recover viability more rapidly after Elesclomol-$CuCl_2$ treatment. In conclusion, *GJB2*-OE mitigates copper-induced cell death in OC cells treated with Elesclomol-$CuCl_2$.

GJB2 inhibits the infiltration of $CD8^+$ T cells and promotes immune escape

The tumor immune microenvironment (TIME) has emerged as a critical focus in cancer research, with growing evidence highlighting its role in tumor progression and therapeutic response. While our previous studies have established that abnormal *GJB2* expression can regulate the malignant progression in OC, its specific impact on immune regulation remains poorly understood. To investigate *GJB2*'s immunomodulatory role, we first applied the TIDE algorithm to assess the potential efficacy of immunotherapy across OC subgroups stratified by *GJB2* expression levels. Given that higher TIDE scores correlate with increased immune evasion and reduced likelihood of benefiting from ICI therapy [42, 43], our analysis revealed that elevated *GJB2* expression in the TCGA cohort was associated with significantly higher TIDE, Dysfunction, and Exclusion scores (Fig. 10A, C). These findings collectively indicate that *GJB2* overexpression may contribute to an immunosuppressive TIME, potentially diminishing immunotherapy responsiveness in OC patients. To further investigate the immunomodulatory role of *GJB2*, we examined its correlation with immunosuppressive components in the tumor microenvironment, including regulatory T cell marker *FOXP3*, M2 macrophage marker *CD163*, and immune checkpoint molecules (*TIGIT*, *CTLA4*, and *CD274*). Strikingly, *GJB2* expression showed significant positive correlations with all these immunosuppressive markers (*FOXP3*, *CD163*, *TIGIT*, *CTLA4*, and *CD274*) (Fig. 10D), strongly suggesting that *GJB2* overexpression contributes to establishing an immunosuppressive tumor microenvironment in OC.

To elucidate the mechanism by which *GJB2* modulates immune cell function, we performed Transwell migration assays which revealed that *GJB2*-overexpressing OC cells exhibited significantly reduced chemotactic attraction of $CD8^+$ T cells compared to controls (Fig. 10E), consistent with its established pro-tumorigenic role. This impaired recruitment capacity suggests that *GJB2* may facilitate immune evasion by inhibiting $CD8^+$ T cell infiltration. Furthermore, in functional co-culture experiments using OTK3-activated primary human $CD8^+$ T cells (effector: target ratio = 5:1), flow cytometric analysis demonstrated that *GJB2* overexpression in tumor cells substantially suppressed the production of key cytokines (Granzyme B and IFN-γ) compared to control cells after 24 h of co-culture (Fig. 10F). These findings collectively demonstrate that *GJB2* not only inhibits $CD8^+$ T cell migration but also functionally impairs their cytotoxic potential, ultimately fostering an immune-evasive tumor microenvironment.

Discussion

Ovarian cancer (OC) is one of the most common malignancies of the genital tract, with high mortality rates and a significant impact on the health of women worldwide [44]. The conventional therapeutic approach for OC typically consists of cytoreductive surgery combined with platinum-based chemotherapy [45]. Nevertheless, a substantial proportion of patients ultimately develop platinum resistance, leading to disease recurrence [46]. Despite advances in characterizing molecular prognostic factors for OC, the field still lacks definitive markers that reliably predict tumor development and serve as clinically useful biomarkers [47]. Therefore, it is crucial to identify promising biomarkers for OC prognosis prediction and to develop effective therapeutic strategies.

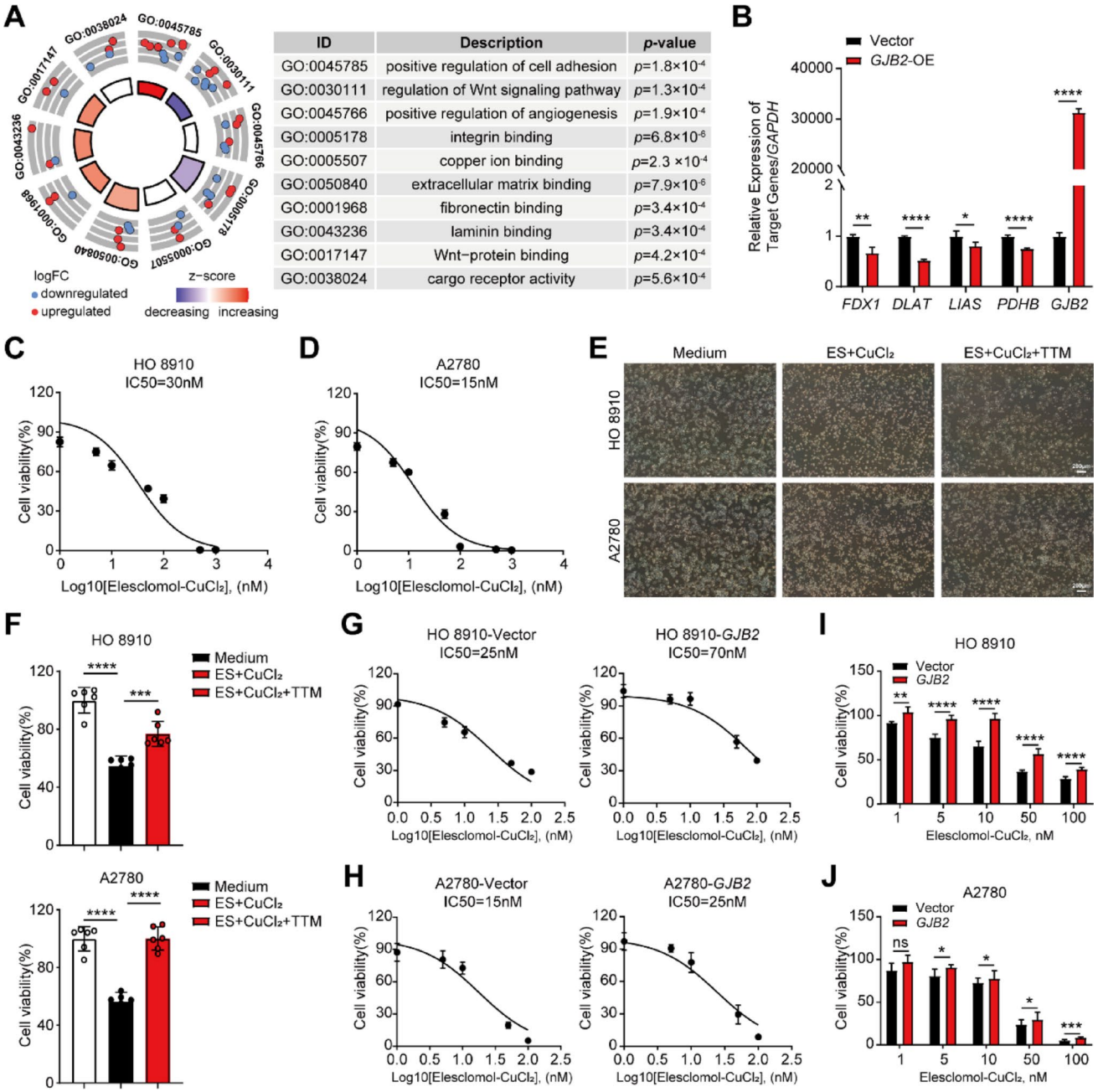

ID	Description	*p*-value
GO:0045785	positive regulation of cell adhesion	$p=1.8\times10^{-4}$
GO:0030111	regulation of Wnt signaling pathway	$p=1.3\times10^{-4}$
GO:0045766	positive regulation of angiogenesis	$p=1.9\times10^{-4}$
GO:0005178	integrin binding	$p=6.8\times10^{-6}$
GO:0005507	copper ion binding	$p=2.3\times10^{-4}$
GO:0050840	extracellular matrix binding	$p=7.9\times10^{-6}$
GO:0001968	fibronectin binding	$p=3.4\times10^{-4}$
GO:0043236	laminin binding	$p=3.4\times10^{-4}$
GO:0017147	Wnt−protein binding	$p=4.2\times10^{-4}$
GO:0038024	cargo receptor activity	$p=5.6\times10^{-4}$

Fig. 9 *GJB2* is Related to Copper Ionophore-induced Cell Death. **A** GO enrichment analysis of signaling pathways associated with *GJB2*-correlated genes ($|R|>0.45$, $p<0.001$). **B** Analysis of *GJB2*, *FDX1*, *DLAT*, *LIAS*, and *PDHB* expression in *GJB2*-overexpressing OC cells by qPCR. **C**–**D** HO 8910 and A2780 cells were exposed to different doses of Elesclomol-$CuCl_2$ for 24 h and detected by CCK-8 reagent. **E** Representative images of OC cells treated with Elesclomol-$CuCl_2$ with or without TTM for 24 h. Scale bars represent 200 μm. **F** The rescue effect of TTM in HO 8910 and A2780 treated with Elesclomol-$CuCl_2$ was explored through CCK-8 assay. **G**–**J** HO 8910 and A2780 cells transfected with *GJB2*-OE were treated with various concentrations of elesclomol for 24 h. Cell viability was evaluated by CCK-8 assay. In all statistical plots, data are expressed as the mean ± SD. *$p<0.05$, **$p<0.01$, ***$p<0.001$, ****$p<0.0001$

In recent years, researchers have focused on developing therapies that induce cancer cell death, as triggering the death of malignant cells is a viable strategy for cancer treatment [48, 49]. Based on different signaling pathways, there are many types of cell death, such as apoptosis, necroptosis, pyroptosis, ferroptosis, and autophagy-dependent cell death [50]. A recent study by Tsvetkov et al. introduced a novel form of copper-induced programmed cell death, termed cuproptosis, which operates through mechanisms distinct from those of classical cell death [11]. Copper, as an essential cofactor for a variety of metalloenzymes that contribute to tumor initiation, invasion, and metastasis [7, 51,

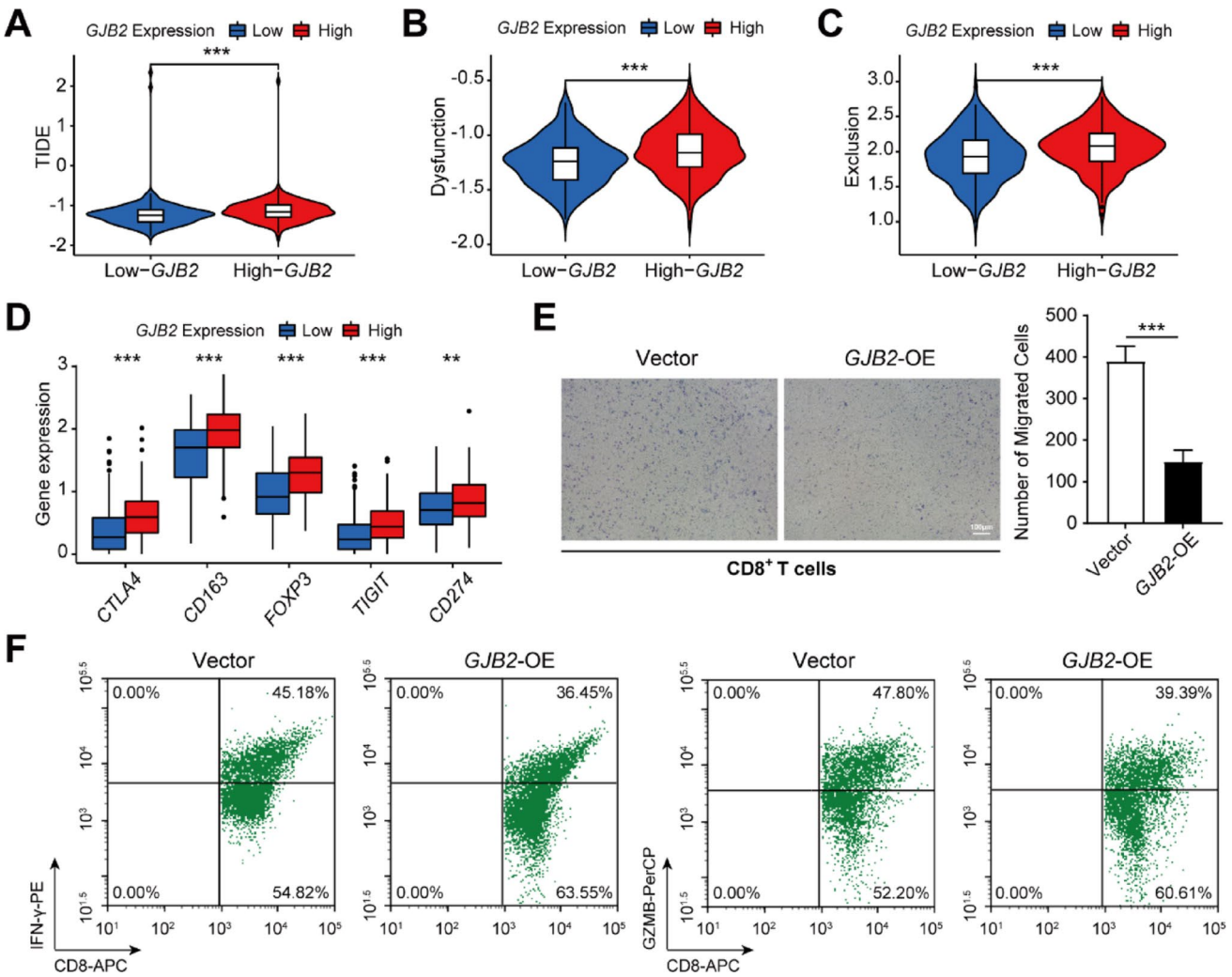

Fig. 10 *GJB2* Inhibits the Infiltration of CD8$^+$ T Cells and Promotes Immune Escape. (A-C) Violin plot illuminating the difference of the TIDE score **A**, Dysfunction score **B**, and Exclusion score **C** between the *GJB2* high- and low-expression groups. **D** Box plot displaying differential expression of immune checkpoints between *GJB2* high- and low-expression groups. **E** CD8$^+$ T cell migration to lower chambers was quantified following *GJB2* overexpression in OC cells. **F** Flow cytometry analysis of Granzyme B (GZMB) and IFN-γ secretion by CD8$^+$ T cells co-cultured with *GJB2*-overexpressing OC cells (E: T ratio = 5:1). In all statistical plots, data are expressed as the mean ± SD. *$p<0.05$, **$p<0.01$, ***$p<0.001$, ****$p<0.0001$

52], has recently emerged as a promising target for developing antitumor therapies. Emerging evidence highlights the critical roles of cuproptosis genes in tumor progression. For example, *LIPT1* significantly influences hepatocellular carcinoma cell proliferation and invasion [53], and *FDX1* induces cuproptosis and regulates anti-tumor immunity in colon cancer [54]. Recent mechanistic studies reveal that copper ions (Cu^+) directly bind to lipoylated *DLAT*, triggering protein aggregation that generates toxic stress and ultimately leads to cuproptosis. Notably, TCA cycle inhibition causes acetyl-CoA accumulation, which competitively suppresses *DLAT* activity and consequently inhibits cuproptosis through feedback regulation [11, 55, 56]. Similarly, *LIAS* gene knockout has been shown to attenuate copper-induced cell death [11]. Likewise, studies in clear cell renal cell carcinoma demonstrate that reduced expression of *PDHB*, a key cuproptosis regulator, is associated with diminished copper-dependent cytotoxicity [57]. Although there is growing interest in the potential connection between cuproptosis and OC, there is currently no direct experimental or clinical evidence to support such a link.

In this work, we enrolled more CRGs to separate OC samples according to the CGs expression levels from public datasets. Using the relevant data of OC patients in TCGA, we constructed a CRG prognosis prediction model based on the regulation of the cuproptosis process. In this research, 5 CRGs (*CD8B2*, *GJB2*, *GRIP2*, *MELK*, and *PLA2G2D*) were chosen to construct a prognostic signature through LASSO Cox regression analysis. OC patients were stratified into high-risk and low-risk groups based on the risk score. The

ROC curve demonstrated the strong predictive performance of the signature. A predictive nomogram was then created by integrating the risk score with clinical factors such as age, grade, and stage, thereby enhancing the model's utility and ease of application. External validation using ICGC cohorts confirmed the robustness of the signature's predictive ability. Functional analyses revealed that CRGs associated with the low-risk and high-risk groups were linked to immune-related pathways. A comparison of immune cell infiltration and activated pathways between the two groups showed that the high-risk group exhibited generally lower levels of infiltrating immune cells and reduced activity of immune-related pathways compared to the low-risk group. Among these 5 signature genes, *GJB2* was associated with the largest number of CGs and showed significant positive associations with critical oncogenic pathways. Studies demonstrate that *GJB2* is highly expressed in various cancers including hepatocellular carcinoma (HCC) [58], non-small cell lung cancer (NSCLC) [59], and breast carcinomas [60], showing significant correlation with poor patient prognosis. Its oncogenic mechanisms involve activation of the NF-κB/HIF-1α/GLUT1/PD-L1 signaling axis, glycolytic regulation, and immune microenvironment remodeling. For instance, in HCC, *GJB2* promotes immune suppression by translocating to the cytoplasm and activating the NF-κB pathway [58], while in NSCLC, its expression can be upregulated by *CAR10* [59]. However, the specific functions and mechanisms of *GJB2* in OC remain unclear and warrant further investigation.

Based on preliminary findings, we prioritized *GJB2* for comprehensive in vitro characterization. Both qPCR assays and bioinformatics analyses revealed that *GJB2* was highly expressed in OC cells and tumor samples, with its elevated expression correlating positively with stage and worse prognosis. Our findings demonstrate that *GJB2* exerts an oncogenic function in OC progression. Silencing *GJB2* markedly suppressed OC cell proliferation and migration, whereas *GJB2* overexpression enhanced these malignant phenotypes and triggered the EMT. Simultaneously, GO enrichment analysis revealed a significant association between *GJB2* and the copper ion binding pathway, with key cuproptosis regulators changed significantly after *GJB2* overexpression. Furthermore, overexpression of *GJB2* weakened the sensitivity of OC cells to cuproptosis. Finally, we demonstrated that *GJB2* markedly suppresses $CD8^+$ T cell infiltration and reduces the secretion of key cytokines (GZMB and IFN-γ), revealing its critical role in promoting immune escape. Our findings establish *GJB2* as a multifunctional oncogenic regulator that may shape the immunosuppressive tumor microenvironment through three distinct mechanisms: promoting regulatory T cell recruitment and M2 macrophage polarization, inhibiting $CD8^+$ T cell infiltration and function, and upregulating immune checkpoint molecule expression. While previous studies have highlighted the role of *GJB2* in cancer progression [13, 14, 61], our study provides new evidence for its specific involvement in OC cuproptosis. *GJB2* was found to interact with the expression of numerous CRGs in OC, both positively and negatively, conjecture that *GJB2* may regulate the cuproptosis process through multiple mechanisms. Nonetheless, additional research is needed to determine the specific regulatory mechanisms by which *GJB2* modulates OC cuproptosis.

These findings suggest the potential clinical application of *GJB2* in the following aspects. Compared to BRCA status (primarily reflecting homologous recombination deficiency) [62], *GJB2* better characterizes tumor proliferative and metastatic potential. Combined analysis of both markers could provide a more comprehensive evaluation of tumor biological characteristics and treatment sensitivity. In contrast to CA-125 (mainly used for clinical diagnosis and treatment monitoring) [63], *GJB2* expression levels objectively indicate tumor malignancy. Integrating both markers significantly improves predictive accuracy for long-term prognosis and therapeutic response. Regarding immunotherapy prediction, high *GJB2* expression shows a significant association with an immunosuppressive microenvironment, suggesting its potential as a predictive biomarker for patient response to immune checkpoint inhibitors.

There may be some possible limitations in the current study. First, the major part of the cohort in this study is derived from the TCGA, GEO, and ICGC databases, which are retrospective studies and need to be validated by prospective analysis. Second, while this study has elucidated the oncogenic mechanisms of *GJB2*, its clinical application requires further validation through large-scale clinical cohorts to verify its predictive value, along with prospective studies to evaluate treatment efficacy based on *GJB2* stratification. Third, none of the anti-GJB2 targeting drugs have been tested in clinical trials to date. As such, the potential immunotherapeutic effects of anti-GJB2 treatment remain speculative. In the future, there is a critical need to develop and evaluate anti-tumor immunotherapeutic agents targeting *GJB2*.

In conclusion, our study elucidates the regulatory mechanisms of cuproptosis in OC, laying the theoretical foundation for developing novel therapies targeting this pathway. Significantly, we not only developed a cuproptosis-related prognostic model for OC but also pinpointed *GJB2* as a key molecular target, a discovery that opens new avenues for targeted therapy and immunotherapy development in OC treatment.

Conclusions

Overall, the prognostic model established in this study holds significant clinical value for guiding targeted therapy and immunotherapy in OC. Our findings identify *GJB2* as a pivotal CRG, whose elevated expression correlates strongly with poor patient outcomes. Functionally, *GJB2* not only promotes OC cell proliferation, migration, and EMT, but also modulates cuproptosis by reducing cellular sensibility to copper-induced cell death. In terms of immune regulation, *GJB2* fosters an immunosuppressive tumor microenvironment by suppressing $CD8^+$ T cell infiltration and cytokine secretion. These discoveries provide novel insights into the regulatory mechanisms of cuproptosis in OC and open new avenues for developing *GJB2*-targeted therapeutic strategies.

Supplementary Information The online version contains supplementary material available at https://doi.org/10.1007/s10495-025-02119-8.

Acknowledgements We sincerely thank the public databases, including TCGA, GTEx, ICGC, GEO, HPA, GEPIA, and KM plotter, for providing open access.

Authors contributions H.L. and G.Y. conceived and guided the study. H.L. mainly took charge of searching the literature, conducting the data analysis and experiments, producing the figures, and writing. G.S. revised the manuscript and conducted the experiments. K.G. downloaded the data from the databases. M.W. and Y.L. organized the data. Z.T., Q.P., and G.Y. revised the manuscript. All authors have read and approved the manuscript.

Funding This work was supported by the National Natural Science Foundation of China [No. 82173376, No. 82372711], and the Natural Science Foundation of Hunan Province [2022JJ70079].

Data availability Data is provided within the manuscript or supplementary information files.

Declarations

Competing interests The authors declare no competing interests.

Ethics approval The study was reviewed and approved by the Ethics Committee of Xiangya Hospital Central South University, approval number 202204081. All clinical samples were collected with informed consent from patients. We declare that all methods are reported in accordance with the declaration of Helsinki.

References

1. Siegel RL, Giaquinto AN, Jemal A (2024) Cancer statistics, 2024. CA Cancer J Clin 74:12–49. https://doi.org/10.3322/caac.21820
2. Kuroki L, Guntupalli SR (2020) Treatment of epithelial ovarian cancer. BMJ 371:m3773. https://doi.org/10.1136/bmj.m3773
3. Wilson MK, Pujade-Lauraine E, Aoki D et al (2017) Fifth ovarian cancer consensus conference of the gynecologic cancer InterGroup: recurrent disease. Ann Oncol 28:727–732. https://doi.org/10.1093/annonc/mdw663
4. Zhang L, Zhao W, Huang J et al (2022) Development of a dendritic cell/tumor cell fusion cell membrane nano-vaccine for the treatment of ovarian cancer. Front Immunol 13:828263. https://doi.org/10.3389/fimmu.2022.828263
5. Marrelli D, Ansaloni L, Federici O et al (2022) Cytoreductive surgery (CRS) and HIPEC for advanced ovarian cancer with peritoneal metastases: Italian PSM oncoteam evidence and study purposes. Cancers (Basel). https://doi.org/10.3390/cancers14236010
6. Yu F, Quan F, Xu J et al (2019) Breast cancer prognosis signature: linking risk stratification to disease subtypes. Brief Bioinform 20:2130–2140. https://doi.org/10.1093/bib/bby073
7. Ge EJ, Bush AI, Casini A et al (2022) Connecting copper and cancer: from transition metal signalling to metalloplasia. Nat Rev Cancer 22:102–113. https://doi.org/10.1038/s41568-021-00417-2
8. Wang Y, Zhang L, Zhou F (2022) Cuproptosis: a new form of programmed cell death. Cell Mol Immunol 19:867–868. https://doi.org/10.1038/s41423-022-00866-1
9. Atakul T, Altinkaya SO, Abas BI et al (2020) Serum copper and zinc levels in patients with endometrial cancer. Biol Trace Elem Res 195:46–54. https://doi.org/10.1007/s12011-019-01844-x
10. Ressnerova A, Raudenska M, Holubova M et al (2016) Zinc and copper homeostasis in head and neck cancer: review and meta-analysis. Curr Med Chem 23:1304–1330. https://doi.org/10.2174/0929867323666160405111543
11. Tsvetkov P, Coy S, Petrova B et al (2022) Copper induces cell death by targeting lipoylated TCA cycle proteins. Science 375:1254–1261. https://doi.org/10.1126/science.abf0529
12. Omori Y, Duflot-Dancer A, Mesnil M et al (1998) Role of connexin (gap junction) genes in cell growth control: approach with site-directed mutagenesis and dominant-negative effects. Toxicol Lett 96–97:105–110. https://doi.org/10.1016/s0378-4274(98)00056-3
13. Naoi Y, Miyoshi Y, Taguchi T et al (2007) Connexin26 expression is associated with lymphatic vessel invasion and poor prognosis in human breast cancer. Breast Cancer Res Treat 106:11–17. https://doi.org/10.1007/s10549-006-9465-8
14. Ezumi K, Yamamoto H, Murata K et al (2008) Aberrant expression of connexin 26 is associated with lung metastasis of colorectal cancer. Clin Cancer Res 14:677–684. https://doi.org/10.1158/1078-0432.Ccr-07-1184
15. Yang J, Qin G, Luo M et al (2015) Reciprocal positive regulation between Cx26 and PI3K/Akt pathway confers acquired gefitinib resistance in NSCLC cells via GJIC-independent induction of EMT. Cell Death Dis 6:e1829. https://doi.org/10.1038/cddis.2015.197

16. Van Campenhout R, Gomes AR, De Groof TWM et al (2021) Mechanisms underlying connexin hemichannel activation in disease. Int J Mol Sci. https://doi.org/10.3390/ijms22073503
17. Wu JI, Wang LH (2019) Emerging roles of gap junction proteins connexins in cancer metastasis, chemoresistance and clinical application. J Biomed Sci 26:8. https://doi.org/10.1186/s12929-019-0497-x
18. Radman BA, Alhameed AMM, Shu G et al (2024) Cellular elasticity in cancer: a review of altered biomechanical features. J Mater Chem B 12:5299–5324. https://doi.org/10.1039/d4tb00328d
19. Teleki I, Krenacs T, Szasz MA et al (2013) The potential prognostic value of connexin 26 and 46 expression in neoadjuvant-treated breast cancer. BMC Cancer 13:50. https://doi.org/10.1186/1471-2407-13-50
20. Goldman MJ, Craft B, Hastie M et al (2020) Visualizing and interpreting cancer genomics data via the Xena platform. Nat Biotechnol 38:675–678. https://doi.org/10.1038/s41587-020-0546-8
21. Hutter C, Zenklusen JC (2018) The cancer genome atlas: creating lasting value beyond its data. Cell 173:283–285. https://doi.org/10.1016/j.cell.2018.03.042
22. Wang Z, Jensen MA, Zenklusen JC (2016) A practical guide to the cancer genome atlas (TCGA). Methods Mol Biol 1418:111–141. https://doi.org/10.1007/978-1-4939-3578-9_6
23. Ma C, Li F, Gu Z et al (2023) A novel defined risk signature of cuproptosis-related long non-coding RNA for predicting prognosis, immune infiltration, and immunotherapy response in lung adenocarcinoma. Front Pharmacol 14:1146840. https://doi.org/10.3389/fphar.2023.1146840
24. Yan T, Yang H, Meng Y et al (2023) Targeting copper death genotyping associated gene RARRES2 suppresses glioblastoma progression and macrophages infiltration. Cancer Cell Int 23:105. https://doi.org/10.1186/s12935-023-02950-6
25. Huang Y, Yin D, Wu L (2022) Identification of cuproptosis-related subtypes and development of a prognostic signature in colorectal cancer. Sci Rep 12:17348. https://doi.org/10.1038/s41598-022-22300-2
26. Mayakonda A, Lin DC, Assenov Y et al (2018) Maftools: efficient and comprehensive analysis of somatic variants in cancer. Genome Res 28:1747–1756. https://doi.org/10.1101/gr.239244.118
27. Ritchie ME, Phipson B, Wu D et al (2015) limma powers differential expression analyses for RNA-sequencing and microarray studies. Nucl Acids Res 43:e47. https://doi.org/10.1093/nar/gkv007
28. Ashburner M, Ball CA, Blake JA et al (2000) Gene ontology: tool for the unification of biology. The gene ontology consortium. Nat Genet 25:25–29. https://doi.org/10.1038/75556
29. Yu G, Wang LG, Han Y et al (2012) clusterProfiler: an R package for comparing biological themes among gene clusters. OMICS 16:284–287. https://doi.org/10.1089/omi.2011.0118
30. Ogata H, Goto S, Sato K et al (1999) KEGG: kyoto encyclopedia of genes and genomes. Nucl Acids Res 27:29–34. https://doi.org/10.1093/nar/27.1.29
31. Hänzelmann S, Castelo R, Guinney J (2013) GSVA: gene set variation analysis for microarray and RNA-seq data. BMC Bioinf 14:7. https://doi.org/10.1186/1471-2105-14-7
32. Pardoll DM (2012) The blockade of immune checkpoints in cancer immunotherapy. Nat Rev Cancer 12:252–264. https://doi.org/10.1038/nrc3239
33. Geeleher P, Cox NJ, Huang RS (2014) Clinical drug response can be predicted using baseline gene expression levels and in vitro drug sensitivity in cell lines. Genome Biol 15:R47. https://doi.org/10.1186/gb-2014-15-3-r47
34. Yang W, Soares J, Greninger P et al (2013) Genomics of drug sensitivity in cancer (GDSC): a resource for therapeutic biomarker discovery in cancer cells. Nucl Acids Res 41:D955-961. https://doi.org/10.1093/nar/gks1111
35. Geeleher P, Cox N, Huang RS (2014) pRRophetic: an R package for prediction of clinical chemotherapeutic response from tumor gene expression levels. PLoS ONE 9:e107468. https://doi.org/10.1371/journal.pone.0107468
36. Asplund A, Edqvist PH, Schwenk JM et al (2012) Antibodies for profiling the human proteome-the human protein atlas as a resource for cancer research. Proteomics 12:2067–2077. https://doi.org/10.1002/pmic.201100504
37. Bi F, Chen Y, Yang Q (2020) Significance of tumor mutation burden combined with immune infiltrates in the progression and prognosis of ovarian cancer. Cancer Cell Int 20:373. https://doi.org/10.1186/s12935-020-01472-9
38. Reardon DA, Gokhale PC, Klein SR et al (2016) Glioblastoma eradication following immune checkpoint blockade in an orthotopic, immunocompetent model. Cancer Immunol Res 4:124–135. https://doi.org/10.1158/2326-6066.Cir-15-0151
39. Rotte A (2019) Combination of CTLA-4 and PD-1 blockers for treatment of cancer. J Exp Clin Cancer Res 38:255. https://doi.org/10.1186/s13046-019-1259-z
40. Buccarelli M, D'Alessandris QG, Matarrese P et al (2021) Elesclomol-induced increase of mitochondrial reactive oxygen species impairs glioblastoma stem-like cell survival and tumor growth. J Exp Clin Cancer Res 40:228. https://doi.org/10.1186/s13046-021-02031-4
41. Gao W, Huang Z, Duan J et al (2021) Elesclomol induces copper-dependent ferroptosis in colorectal cancer cells via degradation of ATP7A. Mol Oncol 15:3527–3544. https://doi.org/10.1002/1878-0261.13079
42. Chen Y, Li ZY, Zhou GQ et al (2021) An immune-related gene prognostic index for head and neck squamous cell carcinoma. Clin Cancer Res 27:330–341. https://doi.org/10.1158/1078-0432.Ccr-20-2166
43. Wu J, Li L, Zhang H et al (2021) A risk model developed based on tumor microenvironment predicts overall survival and associates with tumor immunity of patients with lung adenocarcinoma. Oncogene 40:4413–4424. https://doi.org/10.1038/s41388-021-01853-y
44. Bray F, Laversanne M, Sung H et al (2024) Global cancer statistics 2022: GLOBOCAN estimates of incidence and mortality worldwide for 36 cancers in 185 countries. CA Cancer J Clin 74:229–263. https://doi.org/10.3322/caac.21834
45. Battistini C, Cavallaro U (2023) Patient-derived in vitro models of ovarian cancer: powerful tools to explore the biology of the disease and develop personalized treatments. Cancers (Basel). https://doi.org/10.3390/cancers15020368
46. van Zyl B, Tang D, Bowden NA (2018) Biomarkers of platinum resistance in ovarian cancer: what can we use to improve treatment. Endocr Relat Cancer 25:R303-r318. https://doi.org/10.1530/erc-17-0336
47. Radu MR, Prădatu A, Duică F et al (2021) Ovarian cancer: biomarkers and targeted therapy. Biomedicines. https://doi.org/10.3390/biomedicines9060693
48. Strasser A, Vaux DL (2020) Cell death in the origin and treatment of cancer. Mol Cell 78:1045–1054. https://doi.org/10.1016/j.molcel.2020.05.014
49. Zhang Y, Tang J, Jiang C et al (2025) Metabolic reprogramming in cancer and senescence. MedComm (2026) 6:e70055. https://doi.org/10.1002/mco2.70055
50. Qi X, Li Q, Che X et al (2022) Application of regulatory cell death in cancer: based on targeted therapy and immunotherapy. Front Immunol 13:837293. https://doi.org/10.3389/fimmu.2022.837293

51. Fouani L, Menezes SV, Paulson M et al (2017) Metals and metastasis: exploiting the role of metals in cancer metastasis to develop novel anti-metastatic agents. Pharmacol Res 115:275–287. https://doi.org/10.1016/j.phrs.2016.12.001
52. Shanbhag VC, Gudekar N, Jasmer K et al (2021) Copper metabolism as a unique vulnerability in cancer. Biochim Biophys Acta Mol Cell Res 1868:118893. https://doi.org/10.1016/j.bbamcr.2020.118893
53. Yan C, Niu Y, Ma L et al (2022) System analysis based on the cuproptosis-related genes identifies LIPT1 as a novel therapy target for liver hepatocellular carcinoma. J Transl Med 20:452. https://doi.org/10.1186/s12967-022-03630-1
54. Wang L, Cao Y, Guo W et al (2023) High expression of cuproptosis-related gene FDX1 in relation to good prognosis and immune cells infiltration in colon adenocarcinoma (COAD). J Cancer Res Clin Oncol 149:15–24. https://doi.org/10.1007/s00432-022-04382-7
55. Peng X, Zhao H, Ye L et al (2024) Biomarker identification and risk prediction model development for differentiated thyroid carcinoma lung metastasis based on primary lesion proteomics. Clin Cancer Res 30:3059–3072. https://doi.org/10.1158/1078-0432.Ccr-23-3806
56. Xie J, Yang Y, Gao Y et al (2023) Cuproptosis: mechanisms and links with cancers. Mol Cancer 22:46. https://doi.org/10.1186/s12943-023-01732-y
57. Wang H, Yang Z, He X et al (2023) Cuproptosis related gene PDHB is identified as a biomarker inversely associated with the progression of clear cell renal cell carcinoma. BMC Cancer 23:804. https://doi.org/10.1186/s12885-023-11324-0
58. Liu H, Li X, Zhang C et al (2024) GJB2 promotes HCC progression by activating glycolysis through cytoplasmic translocation and generating a suppressive tumor microenvironment based on single cell RNA sequencing. Adv Sci (Weinh) 11:e2402115. https://doi.org/10.1002/advs.202402115
59. Li S, Liu Y, Qiu G et al (2021) Long non-coding RNA CAR10 facilitates non-small cell lung cancer cell migration and invasion by modulating the miR-892a/GJB2 pathway. Cancer Manag Res 13:1967–1979. https://doi.org/10.2147/cmar.S287386
60. Castellana B, Escuin D, Peiró G et al (2012) ASPN and GJB2 are implicated in the mechanisms of invasion of ductal breast carcinomas. J Cancer 3:175–183. https://doi.org/10.7150/jca.4120
61. Liu X, Furuya T, Li D et al (2010) Connexin 26 expression correlates with less aggressive phenotype of intestinal type-gastric carcinomas. Int J Mol Med 25:709–716. https://doi.org/10.3892/ijmm_00000395
62. Ramus SJ, Gayther SA (2009) The contribution of BRCA1 and BRCA2 to ovarian cancer. Mol Oncol 3:138–150. https://doi.org/10.1016/j.molonc.2009.02.001
63. Krivak TC, Tian C, Rose GS et al (2009) A gynecologic oncology group study of serum CA-125 levels in patients with stage III optimally debulked ovarian cancer treated with intraperitoneal compared to intravenous chemotherapy: an analysis of patients enrolled in GOG 172. Gynecol Oncol 115:81–85. https://doi.org/10.1016/j.ygyno.2009.06.021